

1 **Retrieval of the thickness of undeformed sea ice from**  
2 **Simulated C-band compact polarimetric SAR images**

3

4 X. Zhang<sup>1</sup>, W. Dierking<sup>2</sup>, J. Zhang<sup>1</sup>, J. M. Meng<sup>1</sup>, and H. T. Lang<sup>3</sup>

5 [1]{the First Institute of Oceanography, State Oceanic Administration, Qingdao,  
6 China}

7 [2]{Alfred Wegener Institute for Polar and Marine Research, Bremerhaven,  
8 Germany}

9 [3]{Beijing University of Chemical Technology, Beijing, China}

10 Correspondence to: X. Zhang (zhangxi1981@gmail.com)

11

12 **Abstract.** In this paper we introduce a parameter for the retrieval of the thickness of  
13 undeformed first-year sea ice that is specifically adapted to compact polarimetric (CP)  
14 synthetic aperture radar (SAR) images. The parameter is denoted as “*CP-Ratio*”. In  
15 model simulations we investigated the sensitivity of *CP-Ratio* to the dielectric  
16 constant, ice thickness, ice surface roughness, and radar incidence angle. From the  
17 results of the simulations we deduced optimal sea ice conditions and radar incidence  
18 angles for the ice thickness retrieval. C-band SAR data acquired over the Labrador  
19 Sea in circular transmit, linear receive (CTRL) mode were generated from  
20 RADARSAT-2 quad-polarization images. In comparison with results from

1 helicopter-borne measurements we tested different empirical equations for the  
2 retrieval of ice thickness. An exponential fit between *CP-Ratio* and ice thickness  
3 provides the most reliable results. Based on a validation using other compact  
4 polarimetric SAR images from the same region we found a root mean square (rms)  
5 error of 8 cm and a maximum correlation coefficient of 0.94 for the retrieval  
6 procedure when applying it to level ice between 0.1 m and 0.8 m thick.

7

## 8 **1 Introduction**

9 Sea ice covers about one tenth of the world ocean surface and significantly affects the  
10 exchanges of momentum, heat, and mass between the sea and the atmosphere. Not  
11 only sea ice extent is a significant indicator and effective modulator of regional and  
12 global climate change, but also sea ice thickness is an important parameter from a  
13 thermodynamic and kinematic perspective (Soulis et al., 1989; Kwok, 2010). The  
14 decline of sea ice extent recently observed in the Arctic, e. g. is linked with a decrease  
15 of ice thickness and increasing fractions of seasonal ice areas (e.g. Kwok et al., 2009).  
16 Measurements of sea ice thickness are compared with model results to control and  
17 validate the model capabilities for reproducing recent and predicting future trends of  
18 sea ice conditions in the Arctic (e.g. Laxon et al., 2013). Although sea ice thickness is  
19 only several meters at most, it forms an effective thermal insulation layer due to its  
20 high albedo and low thermal conductivity, leading to a significant reduction in the  
21 heat flux from the ocean to the atmosphere, especially in winter (Vancoppenolle et al.,  
22 2005). Besides investigations focusing on the entire Arctic or Antarctic region, other

1 studies analyze ice thickness variations on local scales to improve regional ice  
2 thickness retrievals (e.g. Haapala et al., 2013). Operational services charged with  
3 providing sea ice maps and forecasting ice conditions for marine transportation and  
4 offshore operations need near-real time regular information about local and regional  
5 ice thickness distributions. The use of sensors providing high spatial resolutions on  
6 the order of 100 meters or better such as SAR for ice thickness retrieval is an  
7 important topic of recent research (Dierking, 2013).

8 Unfortunately, the sea ice thickness distribution is also one of the most difficult  
9 parameter to measure. The most direct and accurate measurement technique is in-situ  
10 drilling with an ice auger. Although it provides data with sufficient accuracy (in the  
11 range of centimeters), it is time consuming and spatially limited. Therefore, this  
12 method is used mainly for calibration of other sensors or methods. To obtain ice  
13 thickness distributions at larger spatial scales, remote sensing methods are requisite  
14 tools. There are generally different strategies:

15 1) Measurements of ice draft using upward-looking sonar on ocean moorings or  
16 submarines (Wadhams, 1980; Behrendt et al., 2013) from which thickness is  
17 estimated based on assumptions about buoyancy, ice density, and snow load (e. g.  
18 Rothrock et al., 1999). Such data provide information about detailed temporal  
19 thickness variations (daily or even hourly) at a fixed location. An example for using in  
20 situ measurements of ice thickness from the New Arctic Program initiated by the  
21 Canadian Ice Service (CIS) starting in 2002, and sea ice draft measurements from  
22 moored ULS instruments in the Beaufort Gyre Observing System for testing a method

1 of ice thickness retrieval from optical methods is provided by Wang et al. (2010).

2 2) Measurements of sea ice freeboard (i.e., the part of the ice above the water level)  
3 plus snow layer thickness with laser altimetry (e. g. Wadhams et al., 1992; Dierking,  
4 1995). From such data, the average ice thickness can be estimated, or the probability  
5 density function (PDF) of ice freeboard can be converted to a PDF of ice thickness.  
6 However, the estimation of ice thickness from freeboard data is less reliable than from  
7 ice draft because of a relatively stronger impact of errors in the freeboard  
8 measurements (Goebell, 2011).

9 3) Measuring the distance between snow surface and ice bottom with electromagnetic  
10 induction sounders (EMS) mounted on sledges, ships or helicopters/airplanes  
11 (Goebell, 2011; Haas et al., 1997; Prinsenberg et al., 2012a, 2012b). With such  
12 systems, spatial ice thickness variations measured at horizontal distances of a few 10  
13 meters were obtained in various regions (Kovacs et al., 1987; Rossiter and Holladay,  
14 1994; Haas et al., 2006; Hendricks et al. 2011).

15 Although ULS and EMS have all contributed greatly to our knowledge about ice  
16 thickness distributions on local and regional scales, such data can be obtained only at  
17 specific locations over a limited time period. Satellite remote sensing, on the other  
18 hand, is useful to monitor ice thickness variations regularly over much larger areas.

19 On a still experimental basis, data of L-band passive microwave sensors, such as for  
20 example the Soil Moisture and Ocean Salinity mission (SMOS) radiometer, have been  
21 employed to retrieve thickness of, sea-ice thinner than about half a meter. The  
22 limitation of this approach is that it is only possible for very high (almost 100%) sea

1 ice concentration and in cold freezing conditions (Tian-Kunze et al., 2014;  
2 Huntemann et al., 2014). Space-borne altimeter has been used primarily to map ice  
3 thickness, and to monitor and study their trends. The capabilities of laser and radar  
4 altimeter systems (such as CryoSat-2 and ICESAT) for measuring ice freeboard have  
5 been extensively investigated during the last decade (e. g. Kwok and Cunningham,  
6 2008; Kwok et al., 2009; Laxon et al., 2013). Compared with radiometers, which  
7 collect data only at a coarse spatial resolution of a few to tens of kilometers (e.g. 25  
8 km for SSM/I 37 GHz data), the spatial resolutions of radar altimeter systems are  
9 about 250 m along-track for CryoSat-2, and a footprint of about 70 m diameter for  
10 ICESAT. The sea ice products derived from altimeters usually focus on large-scale  
11 spatial and temporal variations. While the large-scale ice thickness product is  
12 important for climate research, the support of marine navigation and offshore  
13 operations in polar areas are crucially dependent on precise and reliable sea ice  
14 thickness maps with spatial resolutions better than 1 km.

15 Space-borne synthetic aperture radar (SAR), which operates in the microwave  
16 frequency band, provides all-weather and day-night high-resolution imagery (within a  
17 range of 1-100 m) with 1~3 days' temporal coverage. Hence, SAR is in general very  
18 useful for operational mapping tasks on regional and local spatial scales (Dierking,  
19 2013). The disadvantage of SAR systems is that higher spatial resolutions are linked  
20 with a limited coverage between 10 and 500 km, compared for example to more than  
21 1000 km for passive microwave radiometers. SAR measures the intensity of the radar  
22 signal backscattered from the ice surface and volume at different polarizations. The

1 backscattered intensity depends on the dielectric constant of the ice and small-scale  
2 (mm – dm range) ice properties such as ice surface roughness and air bubble fractions  
3 and sizes. If at least two polarizations are measured simultaneously, the SAR, which is  
4 a coherent device, can also provide the phase difference between the differently  
5 polarized channels. The most recent SAR sensors have polarimetric capabilities. A  
6 fully polarimetric radar transmits and receives both linear horizontal (H) and vertical  
7 (V) polarized electromagnetic waves. Amplitude and phase information of the  
8 backscattered signal are recorded for four transmit/receive polarizations (HH, HV, VH  
9 and VV). This mode is commonly referred to as “quad-pol”. Quad-pol scenes are  
10 usually acquired at very high spatial resolution. A RADARSAT-2 Quad-pol scene has  
11 a spatial resolution of 4.7 m (slant range)  $\times$  5.0 m (azimuth) at a swath width of 25/50  
12 km. Dual-pol scenes contain two polarimetric channels (e.g. HH and HV or VV and  
13 VH). In operational ice-charting services dual-pol scenes are preferred because of  
14 their wider areal coverage (Geldsetzer et al., 2015). The RADARSAT-2 ScanSAR  
15 Wide mode, e.g., can have a swath width of 500 km with 160-72 m (ground range)  $\times$   
16 100 m (azimuth) resolution. Despite their currently very limited coverage, the  
17 quad-pol images are important information sources to understand the scattering  
18 mechanisms of sea ice.

19 Recently a number of investigators noted correlations between ice thickness and the  
20 co-polarization ratio, which is the ratio of measured intensities at VV- and  
21 HH-polarization (here we use VV/HH). The sensitivity between co-polarization ratio  
22 and thin ice thickness has been firstly demonstrated by Onstott (1992), based on

1 C-band radar data from the Eastern Arctic region. Kwok et al. (1995) estimated the  
2 thin ice thickness (0 to 0.1m) from L- and C- band fully polarimetric airborne SAR  
3 data acquired over the Beaufort Sea. Their approach included the training of a neural  
4 network. L-band polarimetric characteristics of ice in the Sea of Okhotsk were  
5 investigated by Wakabayashi et al. (2004), and the L-band co-polarized ratio was used  
6 to estimate ice thicknesses between 0 and 2 m (their Fig. 13). The investigation was  
7 further extended to other sensors, e.g. to the airborne Pi-SAR (X-, and L-band, data  
8 from the Sea of Okhotsk; Nakamura et al., 2009a; Toyota et al., 2009) and to  
9 ENVISAT ASAR, using radar intensity and ice thickness data from 0.2 to 2.5 m, the  
10 latter acquired from a research vessel in the Lützw-Holm Bay Antarctica (Nakamura  
11 et al., 2009b). The good correlations were attributed to the fact that the co-polarized  
12 ratio values are sensitive to the dielectric constants of the ice surface layer which  
13 changes due to the process of desalination during ice growth. The relationship  
14 between relatively thick multi-year ice (thickness between 2 m and 5 m), on the one  
15 hand, and co-polarized correlation and cross-polarized ratio HV/HH or VH/VV, on the  
16 other hand, was also investigated in the Arctic Ocean employing RADARSAT-2 and  
17 TERRASAR-X data (Kim et al., 2012). They found that the degree of depolarization  
18 is linked to the thickness of the MYI as ice surface roughness increases and salinity  
19 decreases.

20 Although the above mentioned parameters derived from polarimetric SAR imagery  
21 have shown the potential for estimating sea-ice thickness under certain conditions,  
22 polarimetric SAR data can presently only be acquired at limited swath-widths. The

1 quad-pol mode on RADARSAT-2, has a swath width of only 25-50 km, as mentioned  
2 above. The swath width of the VV/HH dual-polarization Stripmap mode on  
3 TerraSAR-X is 15 km. Therefore, they are insufficient for operational use which  
4 requires a large-scale coverage (Scheuchl et al., 2004). The limited swath-width also  
5 restricts scientific investigations to local domains. An alternative is to use compact  
6 polarimetry.

7 The methods of generating compact polarimetric (CP) information (explained below)  
8 are based on receiving data at two different polarizations (Souyris et al., 2005; Raney,  
9 2007). Compared with the “traditional” dual-polarization modes described above, CP  
10 data include a greater amount of polarization information (but less than  
11 quad-polarization data). They can cover much greater swath widths compared to  
12 quad-polarization modes due to reduced power consumption and data storage  
13 requirements.

14 The term “CP system” refers to a unique polarization in transmission and coherent  
15 dual-orthogonal polarizations in reception. There are three different CP configurations  
16 (Nord et al., 2009). The first architecture is the “ $\pi/4$  mode” with a slant linear  
17 transmission and horizontal (H) and vertical (V) receptions (Souyris et al., 2005). The  
18 second is the “dual circular (DC) mode”, i.e. transmitting at a single circular  
19 polarization and receiving two orthogonal circular polarizations. The last approach is  
20 circular transmit and linear (H and V) receive (called CTRLR mode). Among these  
21 three compact polarization modes, the latter has been ranked to be the most promising  
22 in terms of performance and receiver complexity. The current Indian RISAT-1, the



1 Japanese ALOS-2 and the planned Canadian RADARSAT Constellation Mission  
2 (RCM) also support the CTRLR mode. According to the description in Geldsetzer et al.  
3 (2015), the coming CTRLR mode of RCM will be particularly tailored to sea ice  
4 applications by offering a medium-resolution mode with a swath width of 350 km and  
5 a resolution of 50 m, a low-noise mode with the same swath width and a resolution of  
6 100 m., or a low-resolution mode with a swath width of 500 km and a resolution of  
7 100 m. Hence, the CTRLR modes of RCM are well suited for operational sea ice  
8 monitoring.

9 However, one apparent disadvantage of the CP mode as compared to dual- or  
10 quad-polarization mode is the fact that the HH, VV, and HV signal combinations are  
11 not directly measured. This means that the co-polarized ratio (Wakabayashi et al.,  
12 2004; Nakamura et al., 2009a; Toyota et al., 2009) and the cross-polarized ratio (Kim  
13 et al., 2012) which are often used as an ice thickness proxy cannot be directly  
14 calculated from CP mode SAR data. Although CP SAR images have been used to  
15 distinguish sea ice types (Dabboor and Geldsetzer, 2014; Charbonneau et al., 2010;  
16 Geldsetzer et al., 2015), to our knowledge there have been no published studies on its  
17 use for ice-thickness detection in the open literature until now. Therefore, in this study,  
18 we considered the CTRLR mode and developed an approach to directly retrieve the  
19 thickness from CP SAR data (hereafter we assume that the CP SAR is operated in  
20 CTRLR mode). The paper is organized as follows: in Sect. 2 we introduce a new  
21 parameter to estimate ice-thickness and demonstrate its sensitivity to different ice  
22 parameters by numerical modeling in Sect. 3. In Sect. 4, an empirical relationship

1 based on a comparison of CP-SAR signatures with ice thickness data obtained from  
 2 electromagnetic induction sounding is presented, and the retrieval performance of this  
 3 algorithm is described. Further discussions and conclusion are presented in Sect. 5.

4

## 5 **2 Model and method**

### 6 **2.1 Full polarimetry and compact polarimetry**

7 The full polarimetric radar scattering return can be represented by the scattering  
 8 matrix  $\mathbf{S}$

$$9 \quad \mathbf{S} = \begin{bmatrix} S_{HH} & S_{HV} \\ S_{VH} & S_{VV} \end{bmatrix} \quad (1)$$

10 where  $S_{pq}$  denotes the  $p$  transmit and  $q$  received linear polarization. In the monostatic  
 11 case and considering that reciprocity can be assumed for sea ice and snow,  $S_{HV}=S_{VH}$ .

12 We use the coherency matrix  $\mathbf{T}$  to evaluate the second-order statistics of the scattering  
 13 matrix  $\mathbf{S}$ . The coherency matrix  $\mathbf{T}$  formed from the elements of the scattering matrix  $\mathbf{S}$   
 14 is

$$15 \quad \mathbf{T} = \frac{1}{2} \begin{bmatrix} \langle |S_{HH} + S_{VV}|^2 \rangle & \langle (S_{HH} + S_{VV})(S_{HH} - S_{VV})^* \rangle & 2\langle (S_{HH} + S_{VV})S_{HV}^* \rangle \\ \langle (S_{HH} - S_{VV})(S_{HH} + S_{VV})^* \rangle & \langle |S_{HH} - S_{VV}|^2 \rangle & 2\langle (S_{HH} - S_{VV})S_{HV}^* \rangle \\ 2\langle S_{HV}(S_{HH} + S_{VV})^* \rangle & 2\langle S_{HV}(S_{HH} - S_{VV})^* \rangle & 4\langle |S_{HV}|^2 \rangle \end{bmatrix} \quad (2)$$

16 where  $*$  denotes the complex conjugate and  $\langle \bullet \rangle$  the ensemble average.

17 We consider the CTRLR mode for which the scattering vectors are given by (e. g. Nord  
 18 et al, 2009)

$$19 \quad \vec{k}_{CTRLR} = [S_{RH} \quad S_{RV}]^T = [S_{HH} - iS_{HV} \quad -iS_{VV} + S_{HV}]^T / \sqrt{2}. \quad (3)$$

1 As usual, the “*R*” denotes that the transmitted polarization is right circular, while “*H*”  
 2 and “*V*” stand for the linear reception. We set

$$3 \quad \Sigma_H = S_{RH} + iS_{RV} \quad \Sigma_V = S_{RH} - iS_{RV}, \quad (4)$$

4 From Eq. (3) it then follows that

$$5 \quad \Sigma_H = S_{HH} + S_{VV} \quad \Sigma_V = S_{HH} - S_{VV} - i2S_{HV}. \quad (5)$$

6 The terms  $\langle |\Sigma_H|^2 \rangle$  and  $\langle |\Sigma_V|^2 \rangle$  can be expressed as

$$7 \quad \begin{aligned} \langle |\Sigma_H|^2 \rangle &= \langle (S_{HH} + S_{VV})(S_{HH} + S_{VV})^* \rangle \\ &= \langle |S_{HH} + S_{VV}|^2 \rangle, \\ \langle |\Sigma_V|^2 \rangle &= \langle (S_{HH} - S_{VV} - i2S_{HV})(S_{HH} - S_{VV} - i2S_{HV})^* \rangle \\ 8 \quad &= \langle (S_{HH} - S_{VV})(S_{HH} - S_{VV})^* \rangle + \langle i2S_{HV}^*(S_{HH} - S_{VV}) \rangle - \langle i2S_{HV}(S_{HH} - S_{VV})^* \rangle + 4|S_{HV}|^2. \quad (6) \\ &= \langle |S_{HH} - S_{VV}|^2 \rangle + \langle i2S_{HV}^*(S_{HH} - S_{VV}) \rangle - \langle i2S_{HV}(S_{HH} - S_{VV})^* \rangle + 4|S_{HV}|^2 \end{aligned}$$

9 Under the assumption of reflection symmetry, the cross- and co-polarized scattering  
 10 coefficients are uncorrelated. This assumption is reasonable for snow and sea ice  
 11 surfaces at various frequencies and for different spatial scales (Souyris et al., 2005).

12 Hence

$$13 \quad \langle S_{HV}^* S_{VV} \rangle = \langle S_{HH} S_{HV}^* \rangle \approx 0. \quad (7)$$

14 and Eq. (6) can be rewritten by the elements of coherency matrix **T**:

$$15 \quad \langle |\Sigma_H|^2 \rangle = \langle |S_{HH} + S_{VV}|^2 \rangle = t_{11} \quad \langle |\Sigma_V|^2 \rangle = \langle |S_{HH} - S_{VV}|^2 \rangle + 4|S_{HV}|^2 = t_{22} + t_{33}. \quad (8)$$

## 16 2.2 X-Bragg model and X-SPM model

17 According to the results obtained by the Cold Region Research and Engineering  
 18 Laboratory (CRREL’88), the typical ranges of RMS height and correlation lengths for

1 smooth level sea ice are 0.02~0.143 cm and 0.669~1.77 cm respectively (Fung, 1994).  
2 For C-band SAR, the small perturbation method (SPM) can be applied for explaining  
3 the surface scattering characteristics from smooth level sea ice. By doing so the  
4 underlying assumption is that the received radar signatures are typical for Bragg  
5 scattering. However, the SPM fails to describe cross-polarization and de-polarization  
6 effects that are observed in real SAR data. In order to overcome these limitations and  
7 to widen the SPM range of validity, an extended Bragg model (termed X-Bragg model)  
8 was presented by Hajnsek et al. (2003). In the X-Bragg model the scattering surface is  
9 composed of rough randomly tilted facets that are large with respect to the  
10 wavelength but small with respect to the spatial resolution of the sensor (for  
11 RADARSAT-2 fine-quad mode, the wavelength is 5.6 cm and the resolution is 8 or 25  
12 m). Scattering from each rough facet is evaluated by employing the SPM, whereby for  
13 the facets a random tilt is assumed which causes both a random variation  $\Delta\theta$  of the  
14 incidence angle  $\theta$  and a random rotation  $\beta$  of the local incidence plane around the line  
15 of sight. In the X-Bragg model, the random incidence angle variation  $\Delta\theta$  is ignored,  
16 and the incidence plane angle of rotation  $\beta$  is assumed to be uniformly distributed in  
17 an interval  $(-\beta_1, \beta_1)$ , where the parameter  $\beta_1$  is used to characterize the large-scale  
18 roughness (del Monaco et al., 2009).  
19 In order to improve the range of validity of the X-Bragg model, different approaches  
20 (termed X-SPM model) were proposed by del Monaco et al. (2009) and Iodice et al.  
21 (2011). In those studies, more realistic distributions of  $\beta$  and  $\Delta\theta$  were derived by  
22 assuming that the range and azimuth facet slopes are Gaussian random variables. The

1 coherency matrix of the X-SPM model ( $\mathbf{T}_{X-SPM}$ ) after ensemble averaging over the  
 2 local incidence angle  $\theta_l$  and rotation angle  $\beta$  can be expressed as follows (del Monaco  
 3 et al., 2009)

$$4 \quad T_{X-SPM} = \rho \begin{bmatrix} \langle |R_S + R_P|^2 \rangle_{|\theta_l} & c_2 \langle (R_S - R_P)(R_S + R_P)^* \rangle_{|\theta_l} & 0 \\ c_2 \langle (R_S + R_P)(R_P - R_S)^* \rangle_{|\theta_l} & cc_2 \langle |R_S - R_P|^2 \rangle_{|\theta_l} & 0 \\ 0 & 0 & ss_2 \langle |R_S - R_P|^2 \rangle_{|\theta_l} \end{bmatrix}, \quad (9)$$

$$5 \quad c_2 = \langle \cos 2\beta \rangle_{|\beta} = -1 + 2cc,$$

$$6 \quad cc_2 = \langle \cos^2 2\beta \rangle_{|\beta} = \frac{\sin^2 \theta}{\sigma^2} + (1 - 2cc) \frac{\sin^2 \theta + \sigma^2}{\sigma^2},$$

$$7 \quad cc = \langle \cos^2 \beta \rangle_{|\beta} = \sqrt{\frac{\pi \sin^2 \theta}{2\sigma^2}} \exp\left\{\frac{\sin^2 \theta}{2\sigma^2}\right\} \text{Erfc}\left\{\sqrt{\frac{\sin^2 \theta}{2\sigma^2}}\right\},$$

$$8 \quad ss_2 = \langle \sin^2 2\beta \rangle_{|\beta} = 1 - cc_2.$$

9 Here,  $\langle \cdot \rangle_{\theta_l}$  means averaging over the local incidence angle;  $\theta_l$  which is used to  
 10 characterize the random slope variations of the facets;  $\langle \cdot \rangle_{|\beta}$  means averaging over the  
 11 rotation angle  $\beta$ ;  $\rho$  includes small scale roughness effects, and  $\sigma$  is the standard  
 12 deviation of the surface slope which is a Gaussian random variable.  $\text{Erfc}\{\cdot\}$  is the  
 13 complementary Gauss error function.  $R_P$  and  $R_S$  are the Bragg scattering coefficients  
 14 perpendicular and parallel to the incident plane, respectively. Both are functions of the  
 15 complex permittivity  $\varepsilon$  and the incidence angle  $\theta$  (Iodice et al., 2011)

$$16 \quad R_S = \frac{\cos \theta - \sqrt{\varepsilon - \sin^2 \theta}}{\cos \theta + \sqrt{\varepsilon - \sin^2 \theta}} \quad R_P = \frac{(\varepsilon - 1)[\sin^2 \theta - \varepsilon(1 + \sin^2 \theta)]}{(\varepsilon \cos \theta + \sqrt{\varepsilon - \sin^2 \theta})^2}. \quad (10)$$

17 In the paper by del Monaco et al. (2009) it is demonstrated that the X-SPM model  
 18 coincides with the X-Bragg model when the standard deviation of the surface slope is  
 19 zero, and that the X-Bragg model can only be applied for standard deviations of the

1 surface slope  $\sigma < 0.1$ . When  $\sigma > 0.1$ , the effects of incidence angle fluctuations, which  
 2 is ignored in the X-Bragg model, is significant (del Monaco et al., 2009). Because of  
 3 its wider range of validity, we used the X-SPM model in our study.

#### 4 **2.3 Inversion model**

5 For ice thickness retrievals we propose to exploit the ratio between  $\langle |\Sigma_V|^2 \rangle$  and  
 6  $\langle |\Sigma_H|^2 \rangle$  (here denoted as the *CP-Ratio*). The *CP-Ratio* can be written as (see Eq. 4)

$$7 \quad CP - Ratio = \frac{\langle |\Sigma_V|^2 \rangle}{\langle |\Sigma_H|^2 \rangle} = \frac{\langle |S_{RH} - iS_{RV}|^2 \rangle}{\langle |S_{RH} + iS_{RV}|^2 \rangle}. \quad (11)$$

8 By relating the *CP-Ratio* to the elements of the coherency matrix given for the  
 9 X-SPM we obtain

$$10 \quad CP - Ratio = \frac{\langle |\Sigma_V|^2 \rangle}{\langle |\Sigma_H|^2 \rangle} = \frac{cc_2 \langle |R_S - R_P|^2 \rangle_{|\theta_i} + ss_2 \langle |R_S - R_P|^2 \rangle_{|\theta_i}}{\langle |R_S + R_P|^2 \rangle_{|\theta_i}} . \quad (12)$$

$$= \frac{\langle |R_S - R_P|^2 \rangle_{|\theta_i}}{\langle |R_S + R_P|^2 \rangle_{|\theta_i}}$$

11 Equation (12) shows that the *CP-Ratio* is controlled by ensemble averages of the  
 12 difference and sum of the Bragg coefficients with respect to the incidence angle. From  
 13 del Monaco et al. (2009), the probability density function for  $\cos\theta_i$  is a normal  
 14 distribution with mean  $\cos\theta$  and standard deviation equal to  $\sigma\sin\theta$ . After averaging  
 15 over variations of the local incidence angle  $\theta_i$ , the *CP-Ratio* is dependent on the  
 16 dielectric constant of the surface  $\varepsilon$ , the incidence angle  $\theta$ , and the standard deviation

1 of the surface slope  $\sigma$ . By using the model of del Monaco et al. (2009), the results of  
2 SAR measurements can be better explained than with the SPM.

3 We calculated the *CP-Ratio* as a function of the standard deviation of surface slope  $\sigma$   
4 assuming  $\varepsilon=3.9+j0.15$  which are suggested in (Fung and Eom, 1982) for first year sea  
5 ice. The results show that the *CP-Ratio* increases with increasing standard deviation  
6 of the surface slope at fixed incidence angles and with increasing incidence angle at  
7 fixed  $\sigma$  (Fig. 1). The relationship between *CP-Ratio* and the dielectric constant is  
8 presented in Fig. 2. When the incidence angle is constant, the *CP-Ratio* reveals  
9 monotonically increasing values with increasing dielectric constant. A similar trend  
10 also can be found in the co-polarization ratio (Iodice et al., 2011). With respect to our  
11 simulated results shown in Figs.1 and 2, it is important to note that the proposed  
12 parameter *CP-Ratio* is sensitive to the variation of the dielectric constant and almost  
13 insensitive to surface slope variations if  $\sigma < 0.15$ .

14 For our analysis we use the fact that a dry snow layer is transparent at C and L  
15 frequencies (meaning that our method is only applicable under freezing conditions),  
16 and we do not consider metamorphosis of the basal snow layer due to brine wicking  
17 effects or due to melt-freeze cycles. We focus on undeformed Arctic young and  
18 first-year ice for which volume scattering is low because of the relatively high ice  
19 salinity, which means that the ice surface is the dominant scattering source. Then the  
20 backscattering coefficients depends on the small-scale surface roughness and the  
21 dielectric constant of the ice surface. Desalination of the ice occurs parallel to its  
22 growth due to brine drainage (Kovacs, 1996). The desalination process causes a

1 decrease of the dielectric constant. Hence the basic idea of our method for retrieving  
2 ice thickness is to relate changes of the dielectric constant to ice thickness growth.  
3 Because the *CP-Ratio* is sensitive to the variation of the dielectric constant, it is  
4 well-suited for detecting changes of the ice thickness of smooth first-year level ice.

5

## 6 **3 A simulation study**

### 7 **3.1 Forward scattering model**

8 In this section, we describe the combined use of an ice growth model and an  
9 electromagnetic scattering model for level sea ice to study sensitivities of *CP-Ratio* to  
10 different ice and radar properties. We applied the scattering model proposed by  
11 (Nghiem et al., 1995) to simulate the sea ice volume scattering and absorption by  
12 brine inclusions. The surface contribution was calculated with the polarimetric  
13 two-scale model (PTSM) (Iodice et al., 2011, 2013) and incoherently added to the  
14 volume term.

15 The sea ice scattering model configuration is presented in Fig. 3. Note that we do not  
16 explicitly include a snow layer (see also section 2.3). The effects of a dry snow layer  
17 are (1) the dielectric contrast between ice and snow is lower than between ice and air,  
18 hence the reflectivity of the ice surface is lower; (2) the radar wavelength in the snow  
19 is shorter than in air, hence the ice surface appears rougher to the radar; (3) the  
20 incidence angle gets steeper (depending on the dielectric constant of the snow), which  
21 (relatively) causes a stronger backscattering. Since we carry out simulations with



1 different dielectric constants (by varying temperature and brine volume fraction),  
2 surface roughness parameters, and radar incidence angles, the results obtained without  
3 snow can be transferred to cases with dry snow layers.

4 In our model, the uppermost layer is air with permittivity  $\epsilon_0$ , the lowermost medium is  
5 seawater with complex permittivity  $\epsilon_2$ , both enclosing the ice layer. The sea ice  
6 background is assumed to be pure ice with complex permittivity  $\epsilon_i$ . The complex  
7 permittivity of brine inclusions is  $\epsilon_b$ , and their fractional volume is  $f_v$ . The relative  
8 permittivity of the sea ice  $\epsilon_{eff}$  is a function of the volume fraction of brine inclusions  
9 (Arcone et al., 1986; Vant et al., 1978). The ice surface roughness is described by the  
10 correlation length  $l$ , rms height  $s$ , and the standard deviation of surface slope  $\sigma$ . The  
11 thickness and surface temperature of the sea ice layer are  $H$  and  $T_0$ , respectively.  
12 Lastly, the magnetic permeability of free space is  $\mu_0$ . Thickness and permittivity of sea  
13 ice are subject to dynamic changes during the ice growth process. The small-scale  
14 surface roughness (on cm-scale) may also vary temporally and spatially. This,  
15 however, can hardly be measured in the field with sufficient spatial density over larger  
16 areas. Here we do neither consider deformation processes causing surface roughness  
17 components on the order of meters. Furthermore, we assume that the scattering  
18 contribution of the ice-water interface can be neglected because of the relatively high  
19 salinity of Arctic young and first-year ice. Very thin ice for which reflections of the  
20 radar waves between surface and bottom have to be considered is excluded from this  
21 study. In our simulations, we do not take a snow cover into account. We restrict our  
22 analysis to temperatures well below freezing point, which means that a dry snow layer

1 would change the incidence angle and the dielectric contrast at the ice surface. In case  
2 of the ice growth simulations described below, the snow has an insulating effect that  
3 changes the rate of ice thickness growth. Hence, various scenarios can be constructed,  
4 which is beyond the scope of this paper, which we regard as a first step towards  
5 developing a methodology for ice thickness retrieval using CP SAR.

6 For ice growth simulations we use a 1-D thermodynamic model developed by Maykut,  
7 (1978, 1982) based on the energy balance equations at the atmosphere-ocean  
8 boundary. The balance of the heat fluxes at the upper surface of the ice can be  
9 expressed as:

$$10 \quad (1-\alpha)F_r - I_0 + F_L - F_E + F_S + F_e + F_C = 0. \quad (13)$$

11 where  $F_r$  is the incident short wave radiation,  $\alpha F_r$  is the short wave radiation reflected  
12 by ice, and  $\alpha$  is the albedo.  $I_0$  is the amount of shortwave radiation absorbed in the  
13 interior of the ice layer,  $F_L$  is the incoming long wave radiation,  $F_E$  is the long wave  
14 radiation emitted by the ice,  $F_S$  is the sensible heat flux, and  $F_e$  is the latent heat flux.  
15 The last term  $F_C$  is the upward conductive heat flux that is the heat from the bottom  
16 interface conducted through the ice to the upper surface. We assume that the  
17 temperature at the ice-water interface is at  $-1.8^\circ\text{C}$ . The equations and parameters used  
18 in this study are listed in Table 1.

19 Substituting the equations and parameters listed in Table 1 into the Eq. (13) and using  
20 the Newton-Raphson iteration method, the sea ice surface temperature  $T_0$  is obtained.  
21 Once  $T_0$  is known,  $F_E$ ,  $F_S$ ,  $F_e$  and  $F_C$  can be easily calculated. A linear temperature  
22 profile within the sea ice layer is assumed. For volume scattering and absorption

1 calculations we use a mean ice temperature ( $T$ ) calculated from the melting  
2 temperature at the ice-water interface temperature ( $T_b = -1.8$  °C) and the ice surface  
3 temperature ( $T_0$ ). Furthermore, the thickness  $H$  (cm), density  $\rho$  ( $\text{kg m}^{-3}$ ), brine volume  
4 fraction  $f_{vb}$ , and permittivity  $\epsilon_{eff}$  of sea ice, which are directly related to the volume  
5 scattering and absorption in the ice, are obtained by the equations given in Table 2.  
6 The ice surface roughness parameters  $s$ ,  $l$  and  $\sigma$  are set to different values considering  
7 the validity range of the X-SPM model (Ulaby et al., 1982; del Monaco et al., 2009;  
8 Iodice et al., 2011).

### 9 **3.2 Simulation results**

10 To assess theoretical possibilities and limitations of ice-thickness measurements by  
11 *CP-Ratio*, we simulated the evolution of ice growth for given temperature and wind  
12 conditions based on the growth model described in Sect. 3.1. The air temperature and  
13 wind speed were set to  $-12^\circ\text{C}$  and  $10.5 \text{ m s}^{-1}$ , respectively, throughout this simulation,  
14 based on reports from the field measurements that are described in section 4 below.  
15 The simulation started at an initial ice thickness of 1.0 cm. A finite difference scheme  
16 was used to calculate the increase of ice thickness at every 1 h step. After executing  
17 about 25 days' simulation, the following parameters were extracted as a function of  
18 time to drive the sea ice scattering model: ice permittivity  $\epsilon_{eff}$ , thickness of ice layer  $H$ ,  
19 and volume fraction of brine inclusions  $f_{vb}$ . For evaluating the rough surface scattering  
20 contribution, we took roughness data reported in Onstott (1992, Table 5-3) who  
21 listed them for different stages of ice growth: (1)  $s=0.031$  cm and  $l=1.26$  cm ( $ks =$

1 0.035,  $kl = 1.4$  for the radar frequency of 5.4 GHz,  $k$  - wavenumber) for dark nilas, (2)  
2  $s=0.12$  cm and  $l=1.45$  cm ( $ks = 0.14$ ,  $kl = 1.6$ ) for light nilas, and (3)  $s=0.11$  cm and  
3  $l=0.54$  cm ( $ks = 0.12$  and  $kl = 0.6$ ) for smooth first-year ice. We note that we will use  
4 these roughness values for first-year ice in general, considering the large variability of  
5 small-scale ice surface roughness. The values are in the validity range of the original  
6 Bragg scattering theory and should hence be fully covered by the X-SPM model  
7 presented in Iodice et al. (2011). The standard deviation of the large-scale slope  $\sigma$  is  
8 ranging according to the validity range of the X-SPM model (Iodice et al., 2011).

9 At this point we note that a systematic relationship between small-scale surface  
10 roughness and ice thickness has never been reported. Weathering effects, melt events,  
11 and snow metamorphism influence the millimeter-to-centimeter ice surface roughness  
12 to a highly variable extent, independent of ice thickness. As we will show below, the  
13 influence of the small scale roughness on *CP-Ratio* is moderate to low, hence the  
14 issue of varying small-scale surface roughness is not very critical.

15 Figure 4 illustrates the simulated sea ice thickness as a function of time, and ice  
16 temperature, and volume fraction of brine inclusions as functions of ice thickness.

17 Figure 4 clearly shows that the volume fraction of of brine inclusions reduces due to  
18 desalination processes as the ice thickness increases.

19 To investigate the dependence of *CP-Ratio* on the radar incidence angle and ice  
20 thickness, the complex scattering coefficients ( $S_{HH}$ ,  $S_{VV}$ , and  $S_{HV}$ ) were computed for  
21 C-band (5.4 GHz) at incidence angles of  $20^\circ$  -  $60^\circ$ . Then the *CP-Ratio* was calculated  
22 from Eq. (12). The relationship between *CP-Ratio* and sea ice thickness at case (3)

1 (first year ice roughness conditions given above) and  $\sigma = 0.1$  is shown in Fig. 5. It  
2 reveals that *CP-Ratio* exhibits a monotonically decreasing trend with growing  
3 ice-thickness at constant incidence angles. It should be noted that the sensitivity of  
4 *CP-Ratio* to vertical ice growth is much higher at smaller ice-thickness values up to  
5 approximately 0.4 m. This can be explained by fact that the ice salinity is calculated  
6 according to the relationship proposed by (Cox and Weeks, 1983). Their  
7 parameterization of salinity as a function of ice thickness reveals a discontinuity at a  
8 thickness of 0.4 m.

9 Figure. 6 and 7 indicate the roughness dependencies of the *CP-Ratio*. In Fig. 6 the  
10 standard deviation of surface slope  $\sigma$  is varied from 0.05 to 0.4 and the small-scale  
11 roughness is fixed at the case 2 roughness condition ( $s=0.12$  cm,  $l=1.45$  cm). When  $\sigma$   
12 is smaller, the effect of the variability of the ice-surface slope on the sensitivity of the  
13 *CP-Ratio* to ice thickness is small; however, at larger values of  $\sigma$  this effect becomes  
14 significant and weakens the capability of *CP-Ratio* to estimate thickness. Given the  
15 same  $\sigma$ -values, the magnitude of *CP-Ratio* is higher at larger than at smaller incidence  
16 angles, while the sensitivity (given by the local slope of the curves) does hardly  
17 change, as depicted in Figure 7, where we show examples for case 2 (moderate) ice  
18 roughness. The sensitivity as a function of ice thickness remains basically the same  
19 for all incidence angles. A larger magnitude of *CP-Ratio* means that it is less affected  
20 by noise (see equation 11). From the results of these simulations, we expect that the  
21 proposed new parameter for thickness retrieval has a strong correlation with the  
22 thickness of smooth undeformed sea ice over all incidence angles, and the sensitivity

1 is larger for thinner ( $<0.4$  m) than for thicker sea ice. At larger incidence angles, the  
2 reduction of the radar wavelength in a snow layer on top of the ice is not a critical  
3 issue, since the effect of the small-scale roughness on *CP-Ratio* is low in this case.  
4 However, the snow layer also changes the incidence angle of the radar beam on the  
5 ice surface, which can have a considerable impact on the thickness retrieval in  
6 particular at thickness values larger than 0.3 to 0.4 m where the slope of the curves  
7 theoretically decreases to a low value (Fig. 7). In practice, this limitation is less  
8 critical as we show below. On first-year sea ice the bottom part of the snow layer can  
9 be saline due to brine wicking, possibly creating a dielectric interface within the snow,  
10 or resulting in brine volumes large enough to influence the radar backscatter (Barber  
11 and Nghiem, 1999; Galley et al., 2009). This may also affect the accuracy of the  
12 thickness retrieval using *CP-Ratio*. Finally, we note that the model simulations  
13 include interactions between the ice surface and the ice-water interface, which result  
14 in oscillations of the CPR for an ice thickness  $< 0.16$  m. In the field measurements  
15 discussed below, this effect was not observed. We assume that the actual ice thickness  
16 is rarely exactly constant over larger areas.

17

## 18 **4 Datasets and experimental results**

### 19 **4.1 Field Study**

20 On 19-20 March 2011, a field program was conducted by the Department of Fisheries  
21 and Oceans Canada (DFO) along the mid-Labrador coast (Fig. 8) (Prinsenberget al.,

1 2012a). As part of the field survey, snow thickness and ice thickness were measured  
2 with a helicopter-borne sensor package which consists of a laser altimeter, an  
3 electromagnetic induction sounder (EMS), and a ground-penetrating radar (GPR). The  
4 laser altimeter provides the distance to the snow or ice surface, whereas the induction  
5 sounder measures the distance from the sensor to the ice-water interface. Hence the  
6 snow-plus-ice thickness can be obtained (Prinsenberget al., 2012a; 2012b).  
7 Comparisons with drill hole data showed that the ice thickness values derived from  
8 such soundings agree well within  $\pm 0.1$  m over flat homogeneous ice (Haas et al., 2006;  
9 Prinsenberget al., 2012b). The accuracy decreases over ridges and deformed ice,  
10 where the maximum thickness can be underestimated by as much as 50 % (Haas et al.,  
11 2006; Prinsenberget al., 2012b). Snow thickness profiles were collected concurrently  
12 with a ground-penetrating radar (GPR) and the laser altimeter measurements. The  
13 ground-penetrating radar which was operated at a frequency of 1 GHz, receives  
14 returns from the ice-snow and air-snow interfaces, though the return from air-snow  
15 surface is very weak. The laser altimetry is superior for defining the air-snow  
16 interface. Therefore, the combination of GPR and laser altimetry allows to retrieve the  
17 snow depth on sea ice. For a 1 GHz GPR system, the minimum detectable snow layer  
18 thickness is 0.12 m and the measurement error is 0.08 m in light dry snow. (Lalumiere,  
19 2006) By subtracting the GPR snow thickness measurements from the EMS snow  
20 plus ice thickness measurements, sea ice thickness can be estimated.

## 1 4.2 Data sets and data processing

2 All data are available on the Website of DFO including pictures, notes and reports of  
3 the survey ([http://www.bio.gc.ca/science/research-recherche/ocean/ice-glace/  
4 data-donnees-eng.php](http://www.bio.gc.ca/science/research-recherche/ocean/ice-glace/data-donnees-eng.php)).

5 During the field survey, four C-band RADARSAT-2 quad-polarization images were  
6 acquired nearly coincident with the DFO airborne survey flight lines (Fig. 8). The  
7 RADARSAT-2 data were provided by the MacDonald, Dettwiler and Associates Ltd  
8 (MDA). Important SAR parameters are listed in Table 3. For our processing we used  
9 the RADARSAT-2 single-look slant range complex format as starting point. A speckle  
10 reduction filter (13×13 Lee filter) and radiometric calibration procedures were applied  
11 for the calculation of the scattering matrix. With the quad-polarization data, the CTRLR  
12 compact polarimetry mode can be generated via Eq. (3). Subsequently the *CP-Ratio*  
13 was extracted by Eq. (11). Lastly, the geometric registration of the simulated CP SAR  
14 images (i.e. their representation in geographical coordinates) was performed based on  
15 longitude and latitude data provided in SAR metadata.

16 Fig. 8 presents the ice condition at the study site, flight paths and four nearly  
17 coincident RADARSAT-2 fine quad-polarization images. Eight EMS profiles were  
18 measured within the coverage of the four SAR images, and the time differences  
19 between the SAR acquisitions and EMS flights are summarized in Table 4. The  
20 images in Fig. 8 show the RADARSAT-2 data overlain with the EMS flight tracks  
21 over the fast ice and drifting pack ice. According to the ice charts, the total ice  
22 concentrations in fast-ice and pack ice regions are 10/10 and 9/10, respectively. The



1 main ice type in land-fast is first-year ice of 70-120 cm in thickness, and the drift ice  
2 region contains grey ice (10-15 cm thick), grey-white ice (15-30 cm), thin first-year  
3 ice (30-70 cm) and again first-year ice 70-120 cm thick. In the drifting ice region  
4 several openings can be seen in the SAR images. The extent of land-fast ice evolves  
5 in the offshore direction and can be visually separated from the pack ice. Most of the  
6 rougher land-fast ice is brighter in the SAR images than the thinner undeformed  
7 land-fast ice. According to the meteorological data archive from Makkovik station  
8 (<http://climate.weather.gc.ca/>), the air temperature was around -9~-17 °C on 15-16  
9 March 2011, and snow fall was registered during 2 days in the period 17-19 March  
10 with average air temperature around -15 °C. So a large fraction of the sea ice was  
11 covered with snow, which can be clearly seen in aerial photos (not shown). On 19-20  
12 March 2011, the average air temperature was around -8~-12°C and the wind speed  
13 around 11~15 ms<sup>-1</sup> (Prinsenberget al., 2012a). Hence the snow can be regarded as dry.  
14 We also note that thermodynamically driven effects on the bottom snow layer such as  
15 brine wicking take place at temperatures higher than -7°C (Barber and Nghiem, 1999)  
16 which means that we can ignore them here for the freshly fallen snow. However, we  
17 do not have any information about elder snow layers changed by metamorphosis  
18 processes, which may have an influence on the effective backscattering signature. Nor  
19 can we exclude that sea ice flooding took place in some smaller areas. Fig. 9 shows  
20 the ice thickness and snow depth profiles of the land-fast and drift ice, indicating that  
21 the ice freeboard was mostly above the water level. The histograms shown in Fig. 9  
22 confirm that the land-fast mean ice thickness is smaller than the one of the drifting

1 pack ice. The percentages of areas with snow thickness above 0.2 m for land-fast and  
2 drift ice are 26.4% and 18.2% respectively. The flight profiles also show that there are  
3 deformed ice or ridges (ice thickness exceeded 2.0 m) in the survey field.

4 A direct comparison between SAR imagery and flight profiles data may cause errors  
5 due to the time differences of the data acquisitions (the time difference between SAR  
6 and flight data is shown in Table 4). In addition, spatial differences may be caused by  
7 the different sampling and spatial resolutions of the measurement instruments. The  
8 sampling rate for EMS and laser is 10 Hz, which, given a typical helicopter survey  
9 speed of 80 mph, corresponds to a spatial sampling interval of about 3-4 m. While the  
10 footprint size of the laser is very small (several centimeters), the footprint of the EMS  
11 is around 20 m at a typical operation height of 5-6 m. For this experiment, the GPR  
12 was configured to a scan rate of approximately 30 scans per second. When flying at  
13 60-80 knots, the ground sample spacing is approximately one sample per 1.0-1.5 m.  
14 Moreover, according to the DFO survey report, the floating ice drifted 1.4-1.8 knots  
15 towards southeast, as measured by ice beacons (Prinsenberget al., 2012a). In order to  
16 mitigate the errors caused by time and spatial resolution differences, we developed the  
17 following processing chain for linking SAR and airborne data.

18 1. The correction of the time difference was only implemented for the drifting ice  
19 region. The boundary between fast ice and drifting pack ice was taken from ice charts  
20 of the Canadian Ice Service (Fig. 8). For the eight EMS profiles, P1, P2, P5, and P7  
21 are in or near the land-fast ice region, whereas P3, P4, P6, and P8 are from the drift  
22 ice zone. With an ice drift speed of 1.5 knots, and drift direction southeast taken from

1 the DFO survey report and considering the respective time differences, the profiles P3,  
2 P4, P6, and P8 are shifted to their approximate positions at the acquisition time of the  
3 SAR images. The shifted profiles are presented in Fig. 8 (dotted line). It should be  
4 noted that 28 hours passed between the acquisition times of the P8 and SAR data, and  
5 the corrected location of P8 is beyond the coverage of the SAR image. Hence P8 was  
6 discarded from further analysis.

7 2. The EMS (ice plus snow) thickness values below 0.1 cm were removed to consider  
8 the measurement accuracy of the EMS. Regions for which only EMS data but no GPR  
9 data are available were also removed.

10 3. Regions with GPR snow thickness values higher than 0.20 m were removed,  
11 because snow layers thinner than 0.20 m are nearly transparent to C-band radar waves,  
12 and the backscatter from the snow surface and volume can be neglected (Hall et al.,  
13 2006).

14 4. By combining the field survey data (ice charts and aerial photos), a visual  
15 interpretation of RADARSAT-2 SAR was made, and regions of open water, land, and  
16 deformed ice were masked in the SAR images. Land was identified using the coastal  
17 line, open water areas were interpreted via backscattering and texture. Deformed ice  
18 was brighter than level ice in single-polarization SAR images, and revealed a higher  
19 entropy, which was extracted using H/A/ $\alpha$  decomposition (Scheuchl et al., 2002). We  
20 emphasize that in step 1 most open water areas are already excluded from further  
21 analysis.

22 5. For ice zones of 50 m in length, averages of different parameters were evaluated.

1 Firstly, we used the  $H/A/\alpha$  unsupervised Wishart classifier to segment the SAR  
2 images, and each patch was regarded a homogeneous ice area with respect to its radar  
3 signature. Then the snow thickness, snow-plus-ice thickness profiles were cut into 50  
4 m long flight track segments. The *CP-Ratio* values were evaluated from the  
5 co-located, drift-corrected, segmented SAR images, provided that the 50 m segment  
6 contained a homogeneous piece of ice. The segment length of 50 m was chosen  
7 according to the spatial resolution of the SAR image. Range and azimuth spacing of a  
8 RADARSAT-2 fine quad-polarization product are  $4.7\text{ m} \times 4.9\text{ m}$  respectively. Since  
9 we applied a  $13 \times 13$  window for speckle reduction (see above), the effective spatial  
10 resolution is about 50 m. For the averages along transects, 13 SAR pixels, 15 EMS  
11 samples and 45 GPR samples were used.

12 6. The sea ice thickness was extracted from the averaged GPR snow depth and EMS  
13 snow-plus-ice thickness values.

14 7. Finally we calculated the *CP-Ratio* from equation (11) using the averaged complex  
15 backscattering coefficients.

16 This processing chain ensures that only level ice is considered for which the EMS  
17 system delivers reliable thickness data with an acceptable accuracy. The total length  
18 of the profile segments that we used in this study amounts to about 16 km (320  
19 samples). Compared with the original data, almost 60% of the data were discarded in  
20 this processing chain (step 1: 17%, step 2: 10%, step 3: 23%, step 4: 10%).

21

### 1 **4.3 Ice thickness retrieval**

2 To investigate the possibility of using the proposed polarimetric parameter *CP-Ratio*  
3 to estimate sea ice thickness from SAR images, we plotted ice thickness values  
4 obtained during the field campaign describe against the corresponding values of  
5 *CP-Ratio* derived from the RADARSAT-2 images in Figure 10 (using all 320  
6 samples). It can be seen that at C-band, the *CP-Ratio* shows a negative trend relative  
7 to the ice thickness as the simulated results given in Sect. 3.2 predicted. Fig. 10  
8 reveals that the highest sensitivity occurs between 0 and 0.5 m and saturates with  
9 thickness values exceeding 1.5 m. As shown in Figs. 5 to 7, the sensitivity should be  
10 smaller for ice thickness exceeding 0.4 m. However, the slope change of the curves at  
11 0.4 m is not as abrupt as in the theoretical curves predicted in Sect. 3.2. This can be  
12 presumably explained by the fact that we average over segments with different values  
13 of ice roughness parameters  $s$ ,  $l$  and  $\sigma$ . We also need to consider that the  
14 salinity-thickness parameterization proposed by Cox and Weeks (1983) includes a  
15 discontinuity in the slope of the salinity curve at a thickness of 0.4 m, which may not  
16 exist in reality.

17 Since our data comprise different incidence angles ( $29^\circ$ ,  $42^\circ$  and  $49^\circ$  at the survey  
18 positions, Table 3), we can construct the relationships between ice-thickness and the  
19 *CP-Ratio* dependent on the incidence angle. We applied two different fits, a linear and  
20 a logarithmic one, to obtain an empirical relationship between the ice thickness and  
21 *CP-Ratio*. The best regression was obtained using a logarithmic function (Fig. 10).  
22 For Fig. 10, the empirical equations and correlation coefficients (CC) are

$$\begin{cases}
\text{CP - Ratio} = 0.04935 - 0.07329\ln(H) & \text{for } 29^\circ \text{ incident angle (CC} = 0.90) \\
\text{CP - Ratio} = 0.06345 - 0.08251\ln(H) & \text{for } 42^\circ \text{ incident angle (CC} = 0.93) \\
\text{CP - Ratio} = 0.07744 - 0.07952\ln(H) & \text{for } 49^\circ \text{ incident angle (CC} = 0.89)
\end{cases} \quad (14)$$

where all data points (320 samples) are used to derive the empirical regressions in the thickness range from 0.1–1.8 m. The reason to include larger ice thickness values is that they can be measured with a larger accuracy, hence leading to a more robust relationship at least for the moderate thickness values between 0.4 and 0.8 m. However, to our knowledge the distribution of *CP-Ratio* due to speckle has not been derived yet which makes it difficult to judge its variation. The smallest values of *CP-Ratio* observed are about 0.03, which may indicate the noise level of *CP-Ratio*. The measured values of *CP-Ratio* for ice thickness values > 0.2 m shown in Fig. 10 are lower than the theoretical computations. This can presumably be explained by the fact that underlying theoretical models are an over-simplification of the actual situation. We note that due to the limitation of sample points, the fit for 49° incident angle is mainly determined by ice thickness values > 0.5 m. We found that the level of the *CP-Ratio* increases as the incidence angle increases at a given value of the sea ice thickness. This observation compares well with the forward simulation studies as shown in Fig. 5. These high correlations enable us to derive reliable thickness information for smooth level ice from radar images assuming winter conditions (dry snow, no brine wicking). The ice thickness can be estimated using an exponential function, which can be described as follows:

$$H = \exp\left[\frac{a - (\text{CP - Ratio})}{b}\right]. \quad (15)$$

1 where  $a$  and  $b$  are the coefficients of the exponential fit.

2 At the next stage, we focused on the RADARSAT-2 images #2 and #3 (which have  
3 the same incidence angle of  $42^\circ$ ) to validate our method. Out of total 320 samples,  
4 159 samples belong to images #2 and #3. According to the principle of independent  
5 sample test, we divided these 159 samples into two data sets in an arbitrary way. The  
6 first set includes 79 samples that are used to fit the model for estimating ice thickness  
7 and the second one comprises 80 samples that serve to retrieve ice thickness and  
8 compare the results with the data from the field campaign. The coefficients  $a$  and  $b$  of  
9 the empirical fit generated from the first data set are 0.068 and 0.077 respectively.  
10 Note that these coefficients are different from those derived in Eq. (14) from the same  
11 two SAR images, because now less points could be used to derive the fit. The fitted  
12 curve and validation results are presented in Fig. 11a and Fig. 11 b, respectively. The  
13 correlation coefficient for the fit shown in Fig 11a is 0.93 for the thickness range from  
14 0.1 to 1.8 m and 0.94 for the thickness range from 0.1 to 0.8. The RMS error and the  
15 relative error between the observed and the estimated ice thickness, shown in Fig. 11b,  
16 are 12 cm and 20% in the thickness range from 0.1–1.8 m, and 8 cm and 17% for 0.1  
17 to 0.8 m. The relative RMS error implies, e.g. that the absolute RMS error is 0.2 m at  
18 an ice thickness of 1.0 m (for the range 0.1 to 1.8 m). Figure 11b also demonstrates  
19 that the error of the retrieved ice thickness is very large at values  $> 0.8$  m which is to  
20 be expected from the theoretical curves, considering the significantly decreased  
21 sensitivity of *CP-Ratio* to larger ice thickness.

22

## 1 **5 Discussion and conclusion**

2 This paper provides a first analysis of sea ice thickness retrieval using compact  
3 polarimetric SAR. We developed a new parameter that we call *CP-Ratio* to estimate  
4 the thickness of undeformed first-year level ice from C-band radar images, under dry  
5 snow conditions (snow depth < 20 cm). Numerical model simulations showed that  
6 this parameter is sensitive to changes of the dielectric constant that are linked to the  
7 growth of sea ice. We developed empirical relationships for the retrieval of level ice  
8 thickness from *CP-Ratios*. For the validation of our results we also employed  
9 RADARSAT-2 images for which thickness values were available. The optimal  
10 regression between *CP-Ratio* and ice thickness was achieved with an exponential fit.  
11 The RMS error was 12 cm, and the relative error amounted to 20% for a thickness  
12 range between 0.1 and 1.8 m, and 8 cm and 17% for the range between 0.1 and 0.8 m.  
13 This indicates that the proposed parameter is very useful for the retrieval of first-year  
14 level ice thickness between 0.1 and 0.8 m.

15 Since the thickness of deformed ice can be underestimated by the EMS measurements  
16 by as much as 50 or 60 % in the worst cases, we could only study the case of level ice.  
17 The capability of CP SAR to retrieve the thickness of deformed ice, which reveals a  
18 larger variation of large-scale roughness with respect to the sensor resolution, needs to  
19 be further discussed and studied.

20 Although our tests are performed on a limited sample of images, our findings  
21 demonstrate that the C-band compact polarimetric SAR has a potential for sea-ice  
22 thickness retrievals over level first-year ice covered by a thin dry snowpack. The issue



1 of environmental factors affecting the retrieval accuracy, e. g. brine wicking in the  
2 snow, or snow layers with different dielectric properties, has to be investigated further  
3 in more detail. The several planned Earth-observing satellite missions supporting  
4 compact polarimetry (e.g. the RCM operated at C-band) will provide the wide swath  
5 coverage necessary for operational sea ice monitoring. Hence our approach  
6 potentially provides a new operational tool for sea ice thickness measurements with a  
7 large areal coverage. In this case, the resulting thickness products are also of interest  
8 for the development, improvement, and validation of forecast models for the  
9 prediction of ice conditions, or of seasonal and climate simulations that consider  
10 Arctic and Antarctic ice conditions.

11

## 12 **Acknowledgment**

13 This study was supported by the National Nature Science Foundation of China under  
14 Grant 41306193, and the R&D Special Foundation for Public Welfare Industry  
15 (201305025). This work was carried out as part of the Dragon-3 Programme (10501)  
16 by the Ministry of Science and Technology of the P. R. China and the European Space  
17 Agency. The authors would like to thank the Canadian Space Agency (CSA) and  
18 MDA for providing the RADARSAT-2 data, and we are very thankful to the  
19 department of Fisheries and Oceans Canada for their support in providing valuable  
20 snow and sea ice field data. We gratefully acknowledge the detailed comments of  
21 Stefan Kern and two anonymous reviewers which helped to considerably improve the  
22 readability of the article.

1

## 2 **References**

3 Arcone, A., Gow, A. G., and McGrew, S.: Structure and dielectric properties at 4.8  
4 and 9.5 GHz of saline ice, *J. Geophys. Res.*, 91, 14281–14303, 1986.

5 Barber, D. G., and Nghiem, S. V.: The role of snow on the thermal dependence of  
6 microwave backscatter over sea ice, *J. Geophys. Res.*, 104, 25789-25803, 1999.

7 Behrendt, A., Dierking, W., Fahrbach, E., and Witte, H.: Sea ice draft in the Weddell  
8 Sea, measured by upward looking sonars, *Earth Syst. Sci. Data*, 5(1), 209-226,  
9 doi:10.5194/essd-5-209-2013, 2013.

10 Charbonneau, F. J., Brisco, B., Raney, R. K., McNairn, H., Liu, C., Vachon, P.,  
11 Vachon, W., Shang, J., DeAbreu, R., Champagne, Merzouki, A., and Geldsetzer, T.:  
12 Compact polarimetry overview and applications assessment, *Can. J. Remote Sens.*,  
13 36, 298–315, 2010.

14 Cox, G. and Weeks, W.: Equations for determining the gas and brine volumes in  
15 sea-ice samples, *J. Glaciol.*, 29, 306–316, 1983.

16 Cox, G. and Weeks, W.: Numerical simulations of the profile properties of  
17 undeformed first-year sea ice during the growth season, *J. Geophys. Res.*, 93,  
18 12449–12460, 1988.

19 Dabboor, M. and Geldsetzer, T.: Towards sea ice classification using simulated  
20 RADARSAT Constellation Mission compact polarimetric SAR imagery, *Remote  
21 Sens. Environ.*, 140, 189–195, 2014.

22 del Monaco, F. D., Quattro, N. D., Iodic, A., and Natale, A.: Extended small

1 perturbation method and retrieval of natural surface parameters, in: Proc. 6th Eur.  
2 Radar Conf., Rome, Italy, 537–540, 2009.

3 Dierking, W.: Laser profiling of the ice surface topography during the Winter Weddell  
4 Gyre Study 1992, *J. Geophys. Res.*, 100, 4807–4820, 1995.

5 Dierking, W.: Sea ice monitoring by synthetic aperture radar, *Oceanography*, 26, 100–  
6 111, doi: 10.5670/oceanog.2013.33, 2013.

7 Fukusako, S.: Thermophysical properties of ice, snow, and sea ice, *Int. J.*  
8 *Thermophys.*, 11, 353–372, 1990.

9 Fung, A. K. and Eom, H. J.: Application of a combined rough surface and volume  
10 scattering theory to sea ice and snow backscatter, *IEEE T. Geosci. Remote Sens.*,  
11 GE-20, 528–536, 1982.

12 Fung, A. K.: *Microwave Scattering and Emission Models and Their Applications.*  
13 Artech House, Boston, London, 1994.

14 Galley, R. J., Trachtenberg, M., Langlois, A., Barber, D. G., and Shafai, L.:  
15 Observations of geophysical and dielectric properties and ground penetrating radar  
16 signatures for discrimination of snow, sea ice and freshwater ice thickness. *Cold*  
17 *Reg. Scie. Technol.*, 57, 29-38. 2009.

18 Geldsetzer, T., Arkett, M., Zagon, T., Charbonneau, F., Yackel, J. J., and Scharien, R.:  
19 All season compact-polarimetry SAR observations of sea ice, *Canadian J. of*  
20 *Remote Sens.*, doi: 10.1080/07038992.2015.1120661, 2015.

21 Goebell, S.: Comparison of coincident snow-freeboard and sea ice thickness profiles  
22 derived from helicopter-borne laser altimetry and electromagnetic induction

1       sounding, *J. Geophys. Res.*, 116, C08018, doi:10.1029/2009JC006055, 2011.

2       Haapala, J., Lensu, M., Dumont, M., Renner, A. H. H., Granskog, M. A., and Gerland,  
3       S.: Small-scale horizontal variability of snow, sea-ice thickness and freeboard in the  
4       first-year ice region north of Svalbard, *Ann. Glaciol.*, 54, doi:  
5       10.3189/2013AoG62A157, 2013.

6       Haas, C., Gerland, S., Eicken, H., and Miller, H.: Comparison of sea-ice thickness  
7       measurements under summer and winter conditions in the Arctic using a small  
8       electromagnetic induction device, *Geophysics*, 62, 749–757, 1997.

9       Haas, C., Hendricks, S., and Doble, M.: Comparison of the sea ice thickness  
10       distribution in the Lincoln Sea and adjacent Arctic Ocean in 2004 and 2005, *Ann.*  
11       *Glaciol.*, 44, 247–252, 2006.

12       Hajnsek, I., Pottier, E., and Cloude, S. R.: Inversion of surface parameters from  
13       polarimetric SAR, *IEEE T. Geosci. Remote Sens.*, 41, 727–744, 2003.

14       Hall, D. K., Kelly, R. E., Foster, J. L., and Chang, A. T.: Estimation of Snow Extent  
15       and Snow Properties. *Encyclopedia of Hydrological Sciences*, 5-55, 2006.

16       Hendricks, S., Gerland, S., Smedsrud, L.H., Hass, C., Pfaffhuber, A., and Nilsen, F.:  
17       Sea-ice thickness variability in Storfjorden, Svalbard, *Ann. Glaciol.*, 52, 61-68,  
18       2011.

19       Huntemann, M., Heygster, G., Kaleschke, L., Krumpen, T., Mäkynen, M., and Drusch,  
20       M.: Empirical sea ice thickness retrieval during the freeze-up period from SMOS  
21       high incident angle observations, *The Cryosphere*, 8, 439–451,  
22       doi:10.5194/tc-8-439-2014, 2014.

1 Iodice, A., Natale, A., and Riccio, D.: Polarimetric two-scale model for soil moisture  
2 retrieval via dual-Pol HH-VV SAR data, *IEEE J. Sel. Top. Appl.*, 6, 1163–1171,  
3 2013.

4 Iodice, A., Natale, A., and Riccio, D.: Retrieval of soil surface parameters via a  
5 polarimetric two-scale model, *IEEE T. Geosci. Remote Sens.*, 49, 2531–2547,  
6 2011.

7 Ji, S. Y., Yue, Q. J., and Zhang, X.: Thermodynamic analysis during sea ice growth in  
8 the Liaodong Bay, *Mar. Environ. Sci.*, 19, 35–39, 2000.

9 Kim, J. W., Kim, D. J., and Hwang, B. J.: Characterization of Arctic sea ice thickness  
10 using high-resolution spaceborne polarimetric SAR data, *IEEE T. Geosci. Remote*  
11 *Sens.*, 50, 13–22, 2012.

12 Kovacs, A., Valleau, N. C., and Holladay, J. S.: Airborne electro- magnetic sounding  
13 of sea ice thickness and sub-ice bathymetry, *Cold Reg. Scie. Technol.*, 14, 289–311,  
14 1987.

15 Kovacs, A.: Sea Ice, Part I.: Bulk Salinity versus Ice Floe Thickness, USA Cold  
16 Regions Research and Engineering Laboratory, CRREL Rep. 97, United States  
17 Army, Corps of Engineers, 1–16, 1996.

18 Kwok, R., and Cunningham, G. F.: ICESat over Arctic sea ice: Estimation of snow  
19 depth and ice thickness, *J. Geophys. Res.*, 113, C08010, doi:  
20 10.1029/2008JC004753, 2008.

21 Kwok, R., Cunningham, G. F., Wensnahan, M., Rigor, I., Zwally, H. J., and Yi, D.:  
22 Thinning and volume loss of the Arctic Ocean sea ice cover: 2003–2008, *J.*

1 Geophys. Res., 114, C07005, doi: 10.1029/2009JC005312, 2009.

2 Kwok, R., Nghiem, S. V., Yueh, S. H., and Huynh, D. D.: Retrieval of thin ice  
3 thickness from multifrequency polarimetric SAR data, *Remote Sens. Environ.*, 51,  
4 361–374, 1995.

5 Kwok, R.: Satellite remote sensing of sea ice thickness and kinematics: a review, *J.*  
6 *Glaciol.*, 56, 1129-1140, 2010.

7 Lalumiere, L.: Ground penetrating radar of helicopter snow and ice surveys, *Can.*  
8 *Tech. Rep. Hydrogr. Ocean Sci.*, 248, 1–50,  
9 [http://publications.gc.ca/collections/collection\\_2015/mpo-dfo/Fs97-18-248-eng.pdf](http://publications.gc.ca/collections/collection_2015/mpo-dfo/Fs97-18-248-eng.pdf),  
10 2006.

11 Laxon, S. W., Giles, K. A., Ridout, A. L., Wingham, D. J., Willatt, R., Cullen, R.,  
12 Kwok, R., Schweiger, A., Zhang J., Haas, C., Hendricks, S., Krishfield, R., Kurtz,  
13 N., Farrell, S. and Davidson, M.: CryoSat-2 estimates of Arctic sea ice thickness  
14 and volume, *Geophys. Res. Lett.*, 40, 732–737, doi: 10.1002/grl.50193, 2013.

15 Maykut, G. A.: Energy exchange over young sea ice in the central Arctic, *J. Geophys.*  
16 *Res.*, 83, 3646–3658, 1978.

17 Maykut, G. A.: Large-scale heat exchange and ice production in the central Arctic, *J.*  
18 *Geophys. Res.*, 87, 7991–7984, 1982.

19 Nakamura, K., Wakabayashi, H., Naoki, K., Nishio, F., Moriyama, T., and Uratsuka,  
20 S.: Observation of sea-ice thickness in the sea of Okhotsk by using dual-frequency  
21 and fully polarimetric airborne SAR (Pi-SAR) data, *IEEE T. Geosci. Remote Sens.*,  
22 43, 2460–2469, 2009a.

1 Nakamura, K., Wakabayashi, H., Uto, S., Ushio, S., and Nishio, F.: Observation of  
2 sea-ice thickness using ENVISAT data from Lützow- Holm Bay, East Antarctica,  
3 IEEE Geosci. Remote Sens. Lett., 6, 277-281, 2009b

4 Nghiem, S. V., Kwok, R., Yueh, S. H., and Drinkwater, M. R.: Polarimetric signatures  
5 of sea ice, theoretical model, J. Geophys. Res., 100, 13665–13679, 1995.

6 Nord, M. E., Ainsworth, T. L., Lee, J. S., and Stacy, N. J. S.: Comparison of compact  
7 polarimetric synthetic aperture radar modes, IEEE T. Geosci. Remote Sens., 47,  
8 174–188, 2009.

9 Onstott, R.: SAR and scatterometer signatures of sea ice, in Microwave Remote  
10 Sensing of Sea Ice, Geophysical Mono. 68, Carsey, F., Ed., Washington, DC: Amer.  
11 Geophys. Union, pp. 73–104, 1992.

12 Prinsenber, S. J., Peterson, I. K., Holladay, J. S., and Lalumiere, L.: Labrador shelf  
13 pack ice and iceberg survey, March 2011, Can. Tech. Rep. Hydrogr. Ocean Sci.,  
14 275, 1–44, <http://www.ocean-sci.net/275/1/2012/>, 2012a.

15 Prinsenber, S., Holladay S., and Lee J.: Measuring ice thickness with EISflow, a  
16 fixed-mounted helicopter electromagnetic-laser system, Proc. 12th International  
17 Off-shore and Polar Engineering Conference, Kitakyushu, Japan, 737-740, 2012b.

18 Raney, R.: Hybrid polarity SAR architecture, IEEE T. Geosci. Remote Sens., 45,  
19 3397–3404, 2007.

20 Rossiter, J. R., and Holladay, J. S.: Ice-thickness measurement, in Remote Sensing of  
21 Sea Ice and Icebergs, edited by Haykin, S. et al., pp. 141–176, John Wiley,  
22 Hoboken, N. J., 1994.

- 1 Rothrock, D. A., Yu, Y., and Maykut, G. A.: Thinning of the Arctic sea-ice cover,  
2 Geophys. Res. Lett., 26, 3469–3472, doi: 10.1029/1999GL010863, 1999.
- 3 Scheuchl, B., Flett, D., Caves, R., and Cumming, I.: Potential of RADARSAT-2 data  
4 for operational sea ice monitoring, Canadian J. of Remote Sens., 30, 448-461,  
5 2004.
- 6 Scheuchl, B., Hajnsek, I., and Cumming, I.: Sea ice classification using  
7 multi-frequency polarimetric SAR data, in: Geosci. Remote Sens. Symposium,  
8 IGARSS'02, Toronto, Canada, 1914-1916, 2002.
- 9 Soulis, E. D., Lennox, W. C., and Sykes, J. F.: Estimation of the thickness of  
10 undeformed first year ice using radar backscatter, in: Geosci. Remote Sens.  
11 Symposium, IGARSS'89, Vancouver, Canada, 2366–2369, 1989.
- 12 Souyris, J. C., Imbo, P., Fjortoft, R., Mingot, S., and Lee, J. S.: Compact polarimetry  
13 based on symmetry properties of geophysical media: The  $\pi/4$  mode, IEEE T. Geosci.  
14 Remote Sens., 43, 634–646, 2005.
- 15 Tian-Kunze, X., Kaleschke, L., Maaß, N., Mäkynen, M., Serra, N., Drusch, M., and  
16 Krumpfen, T.: SMOS-derived thin sea ice thickness: algorithm baseline, product  
17 specifications and initial verification, The Cryosphere, 8, 997-1018,  
18 doi:10.5194/tc-8-997-2014, 2014.
- 19 Toyota, T., Nakamura, K., Uto, S., Ohshima, K. I., and Ebuchi, N.: Retrieval of sea ice  
20 thickness distribution in the seasonal ice zone from airborne L-band SAR, Int. J.  
21 Remote Sens., 30, 3171–3189, 2009.
- 22 Ulaby, F. T., Moore, R. K., and Fung, A. K.: Microwave Remote Sensing: Active and



- 1 Passive, vols. II, Addison-Wesley, Reading, MA, 1982.
- 2 Vancoppenolle, M., Fichefet, T., and Bitz, C. M.: On the sensitivity of undeformed  
3 Arctic sea ice to its vertical salinity profile, *Geophys. Res. Lett.*, 32, L16502,  
4 doi:10.1029/2005GL023427, 2005.
- 5 Vant, M. R., Ramseier, R. O., and Makios, V.: The complex dielectric constant of sea  
6 ice at frequencies in the range 0.1 to 40 GHz, *J. Appl. Phys.*, 49, 1264–1280, 1978.
- 7 Wadhams, P., Tucker III, W. B., Krabill, W. B., Swift, R. N., Comiso, J. C., and Davis,  
8 N. R.: Relationship between sea ice freeboard and draft in the Arctic Basin, and  
9 implications for ice thickness monitoring, *J. Geophys. Res.*, 97, 20325–20334, doi:  
10 10.1029/92JC02014, 1992.
- 11 Wadhams, P.: A comparison of sonar and laser profiles along corresponding tracks in  
12 the Arctic Ocean, in: *Sea Ice Processes and Models*, edited by: Pritchard, R. S.,  
13 Univ. of Washington Press, Seattle, Wash., 283–299, 1980.
- 14 Wakabayashi, H., Matsuoka, T., and Nakamura, K.: Polarimetric characteristics of sea  
15 ice in the Sea of Okhotsk observed by airborne L-band SAR, *IEEE T. Geosci.*  
16 *Remote Sens.*, 42, 2412–2425, 2004.
- 17 Wang, X., Key, J. R., and Liu, Y.: A thermodynamic model for estimating sea and lake  
18 ice thickness with optical satellite data, *J. Geophys. Res.*, 115, C12035, doi:  
19 10.1029/2009JC005857, 2010.
- 20 Yue, Q. J., Ji, S. Y., Miao, W. D., and Wu, S. L.: Solar radiation on sea ice in Liaodong  
21 Bay, *Oceanol. ET Limnol. Sin.*, 31, 562–567, 2000.

1 Table 1. Equations and parameters used for the sea ice thermodynamic model

Term	Equations	Parameters	Comments
The incident short wave radiation	$F_r = (1 - 0.0065C^2)Q_{so}a^m$ (Ji et al., 2000; Yue et al., 2000)	$a^m = 0.99 - 0.17m$ $m = 0.83$ $C$ in the range 0~1	$a^m$ is the atmospheric transmissivity; $C$ is the cloud coverage; $Q_{so}$ is the solar irradiance for the $D^{\text{th}}$ day in a year; $I_s$ is the solar radiation constant (unit: $\text{W/m}^2$ );
	$Q_{so} = Q_s (\sin\beta \sin\delta + \cos\beta \cos\delta \cos H_a)$ (Yue et al., 2000)	$Q_s = I_s (1 + 0.033 \cos(2\pi D/365))$ $\delta = 23.44^\circ \cos[(172 - D)2\pi/365]$ $H_a = 15(t - 12)\pi/180 + \lambda$	$\delta$ is the declination angle of the sun; $H_a$ is the local solar hour angle; $\beta$ and $\lambda$ are the latitude and longitude; $t$ is Coordinated Universal Time.
The long wave radiation	$F_E = \varepsilon_i \sigma T_0^4$ (Maykut, 1978)	$\sigma = 5.670 \times 10^{-8}$ $\varepsilon_i = 0.97$	$\sigma$ is the Stefan-Boltzman constant (unit: $\text{w}/(\text{m}^2\text{K}^4)$ ); $T_0$ is the surface temperature of sea ice (unit: K); $T_a$ is the air temperature (unit: K);
	$F_L = (1 + kC^2)\varepsilon_a \sigma T_a^4$ (Maykut, 1978)	$k = 0.0017$ $\varepsilon_a = 0.55 + e \times 0.052^{1/2}$	$\varepsilon_i$ is the emissivity of sea ice; $\varepsilon_a$ is the emissivity of atmosphere; $e$ is the water vapor pressure at $T_a$ (unit: HPa).
The sensible heat flux	$F_s = \rho_a C_p C_s u (T_a - T_0)$ (Cox and Weeks, 1988)	$\rho_a = 1.3$ $C_p = 1006$ $C_s = 0.003$	$\rho_a$ is the air density (unit: $\text{kg}/\text{m}^3$ ); $C_p$ is the specific heat at constant pressure (unit: $\text{J}/(\text{kg}\cdot\text{K})$ ); $C_s$ is the sensible heat transfer coefficient; $u$ is the wind speed;
	$F_e = \rho_a L C_e u (q_a - q_0)$ (Cox and Weeks, 1988)	$C_e = 0.00175$ $L = 2.5 \times 10^6 - 2.274 \times 10^3 (T_a - 273.15)$	$L$ is the latent heat of vaporization (unit: $\text{J}/\text{kg}$ );
The latent heat flux	$q_a - q_0 = \frac{0.622}{p_0} \left[ a(fT_a^4 - T_0^4) + b(fT_a^3 - T_0^3) + c(fT_a^2 - T_0^2) + d(fT_a - T_0) + e(f - 1) \right]$ (Cox and Weeks, 1988)	$p_0 = 1013$ $a = 2.7798202 \times 10^{-6}$ $b = -2.6913393 \times 10^{-3}$ $c = 0.97920849$ $d = -158.63779$ $e = 9653.1925$	$p_0$ is the surface atmospheric pressure (unit: mbar); $f$ is the relative humidity; $a, b, c, d,$ and $e$ are constants; $a$ (unit: $\text{k}^4$ ), $b$ (unit: $\text{k}^3$ ), $c$ (unit: $\text{k}^2$ ), $d$ (unit: $\text{k}$ )
	The albedo of sea	$\alpha = \beta_0 + \beta_1 H + \beta_2 H^2 + \beta_3 H^3$ (Cox and Weeks, 1988)	$\beta_0 = 0.2386$ ; $\beta_1 = 6.015 \times 10^{-3}$ ; $\beta_2 = -4.882 \times 10^{-5}$ ;

ice		$\beta_3=1.267 \times 10^{-7}$	
The absorbed shortwave radiation	$I_0=i_0(1-\alpha)F_r$ (Maykut, 1978; Cox and Weeks, 1988)	$i_0=17\%$	$i_0$ is the percent.
The upward conductive heat flux	$F_C = (k/H)(T_b-T_0)$ (Cox and Weeks, 1988)	$k = k_i(1-f_{vb}) + k_b f_{vb}$ $k_i = 4.17 \times 10^4 [5.35 \times 10^{-3} - 2.568 \times 10^{-5}(T_0 - 273.15)]$ $k_b = 4.17 \times 10^4 [1.25 \times 10^{-3} + 3.0 \times 10^{-5}(T_0 - 273.15) + 1.4 \times 10^{-7}(T_0 - 273.15)^2]$ $T_b = -1.8$	$k, k_i, k_b$ are the conductivity of ice layer, pure ice and pure brine, respectively (unit: W/m/K); $T_b$ is the freezing point at 35 salinity (unit: °C); $f_{vb}$ is volume fraction of sea ice brine inclusion.

1

2 Table 2. Equations and parameters used for the sea ice properties

Term	Equations	Parameters	Comments
The ice thickness	$\frac{\Delta h}{\Delta t} = \frac{F_C(H)}{\rho L_f}$ (Cox and Weeks, 1988) $H = \sum_{i=0}^{Time} \frac{\Delta h}{\Delta t} \Delta Time$	$L_f=4.187 \times 10^3(79.6 - 0.505T_b - 0.0273S_i) + 4.3115S_i - T_b + 8 \times 10^{-4} T_b S_i - 0.009(T_b)^2$ (Fukusako, 1990)	$\frac{\Delta h}{\Delta t}$ is the sea ice growth rate when ice thickness is $H$ (unit: m/s); Ice thickness is the sum of ice growth rate. $\Delta Time$ is the time lag (unit: hour).
The sea ice density and brine volume fraction	$\left\{ \begin{array}{l} \rho = \frac{\rho_i F_1(T_i)}{F_1(T_i) - \rho_i S_i F_2(T_i)} \\ f_{vb} = \frac{\rho_i S_i}{F_1(T_i) - \rho_i S_i F_2(T_i)} \end{array} \right.$ (Cox and Weeks, 1983)	$\rho_i=0.917-1.403 \times 10^{-4} T_i$	$\rho$ is sea ice density (unit: kg/m <sup>3</sup> ); $f_{vb}$ is the relative brine volume fraction $\rho_i$ is pure ice density (unit: kg/m <sup>3</sup> ); $T_i$ is the temperature of sea ice (unit: °C); $T_a$ is the air temperature (unit: K); $S_i$ is ice salinity. The functional forms of $F_1$ and $F_2$ can be found from the work of Cox and Weeks (1983).
The ice salinity	$\left\{ \begin{array}{l} S_i = 14.24 - 19.39H \quad (H \leq 0.4 \text{ m}) \\ S_i = 7.88 - 1.59H \quad (H > 0.4 \text{ m}) \end{array} \right.$		$H$ is the ice thickness (unit: m).

(Cox and Weeks, 1983)

The permittivity of sea ice at C-band	$\epsilon'_{eff} = 3.05 + 0.0072f_{vb}$ $\epsilon''_{eff} = 0.02 + 0.0033f_{vb}$ (Arcone et al., 1986; Vant et al., 1978)	$f_{vb}$ is the relative brine volume fraction.
---------------------------------------	--	---

1 Table 3. Specifications of the qual-pol RADARSAT-2 SAR data

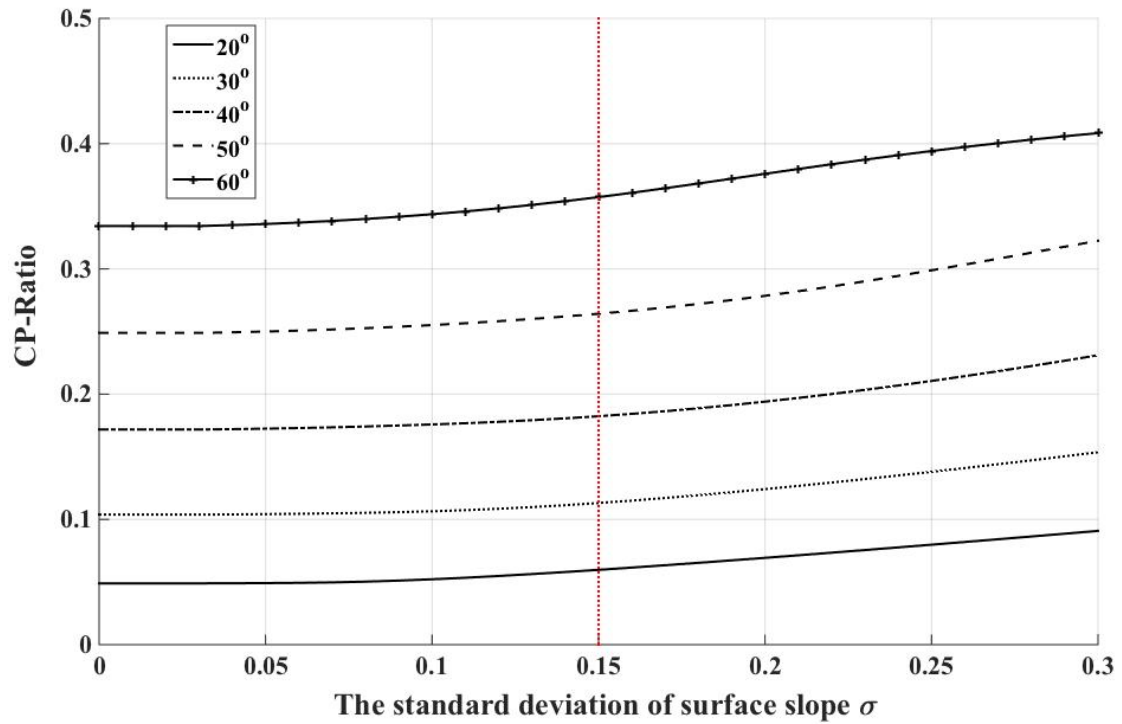
Scene ID	Date/Time (UTC)	Resolution (m)* Rng $\times$ Az	Incidence angle(Deg.)	Beam Mode
#1	19 Mar 2011, 10:25	5.2 $\times$ 7.7	29.0	FQ9
#2	19 Mar 2011, 21:51	5.2 $\times$ 7.7	42.0	FQ23
#3	19 Mar 2011, 21:51	5.2 $\times$ 7.7	42.0	FQ23
#4	20 Mar 2011, 09:56	5.2 $\times$ 7.7	49.0	FQ31

2 \*Resolution is nominal. Ground range resolution varies with incidence angle.

3 Table 4. Specifications of helicopter-borne EMS ice thickness data sets

EM ID	SAR Scene ID coincident with EMS	Date/Time (UTC)	Time difference
P-1	#1	19 Mar 2011 17: 00-17: 20	~ 7 hour
P-2	#2	19 Mar 2011 17: 25-17: 30	~4 hour
P-3	#2	19 Mar 2011 18: 30-18: 45	~3.3 hour
P-4	#3	19 Mar 2011 18: 40-18: 50	~ 3 hour
P-5	#4	20 Mar 2011 11: 55-12: 05	~ 2 hour
P-6	#4	20 Mar 2011 12: 10-12: 25	~ 2.5 hour
P-7	#1	20 Mar 2011	~ 28 hour

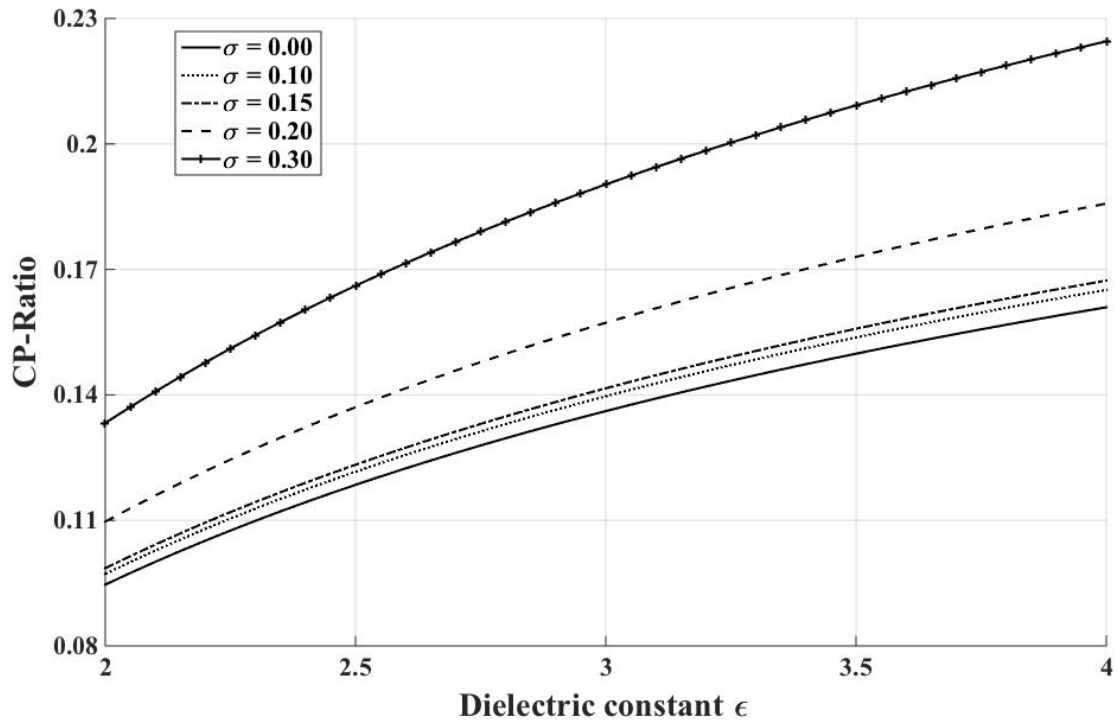
1



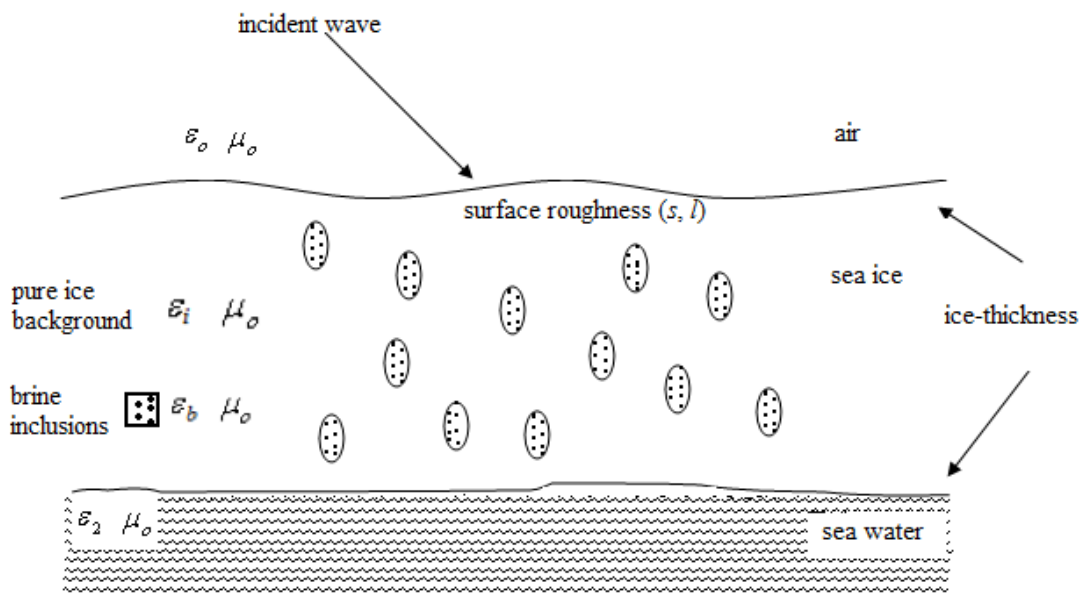
2

3 Figure 1. Variations of *CP-Ratio* as a function of the standard deviation of surface  
 4 slope  $\sigma$  for different incidence angles and  $\epsilon=3.9+j0.15$ . The red line marks the  
 5 maximum threshold of  $\sigma$  for the validity of our approach.

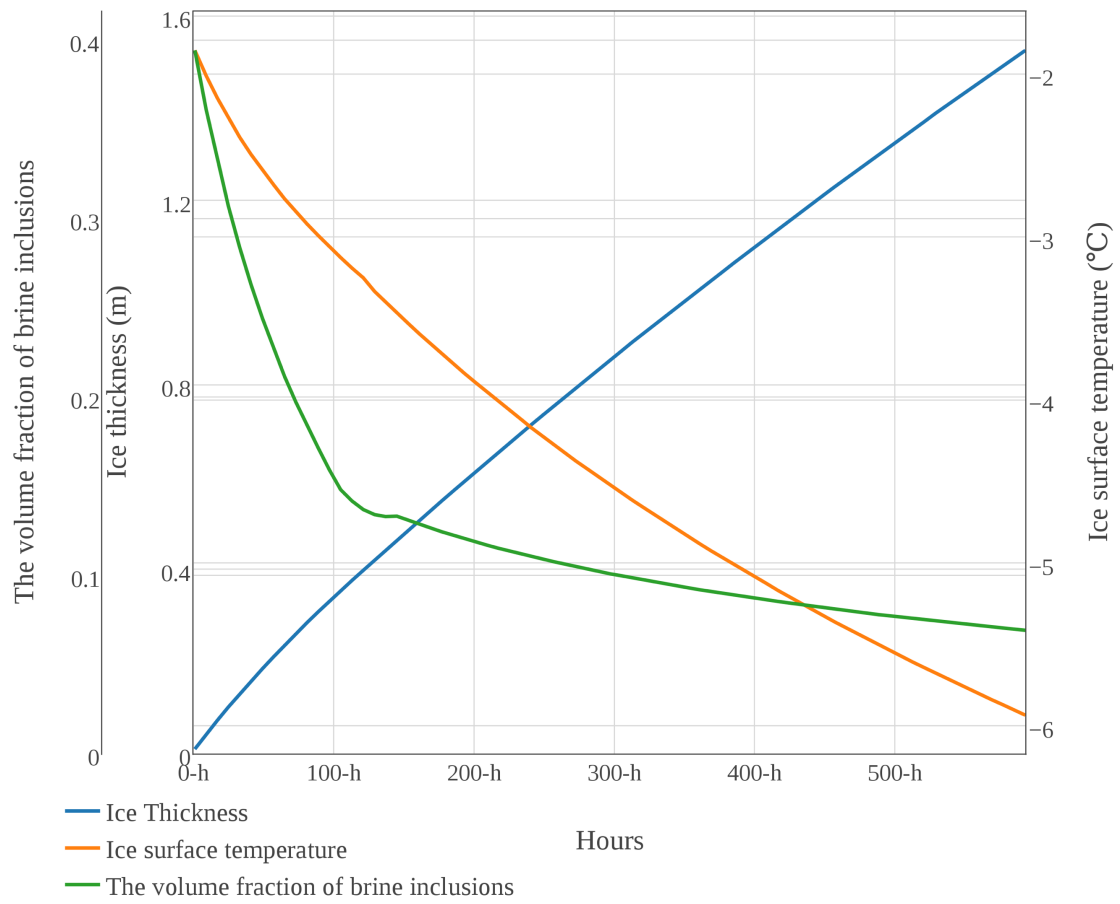
6



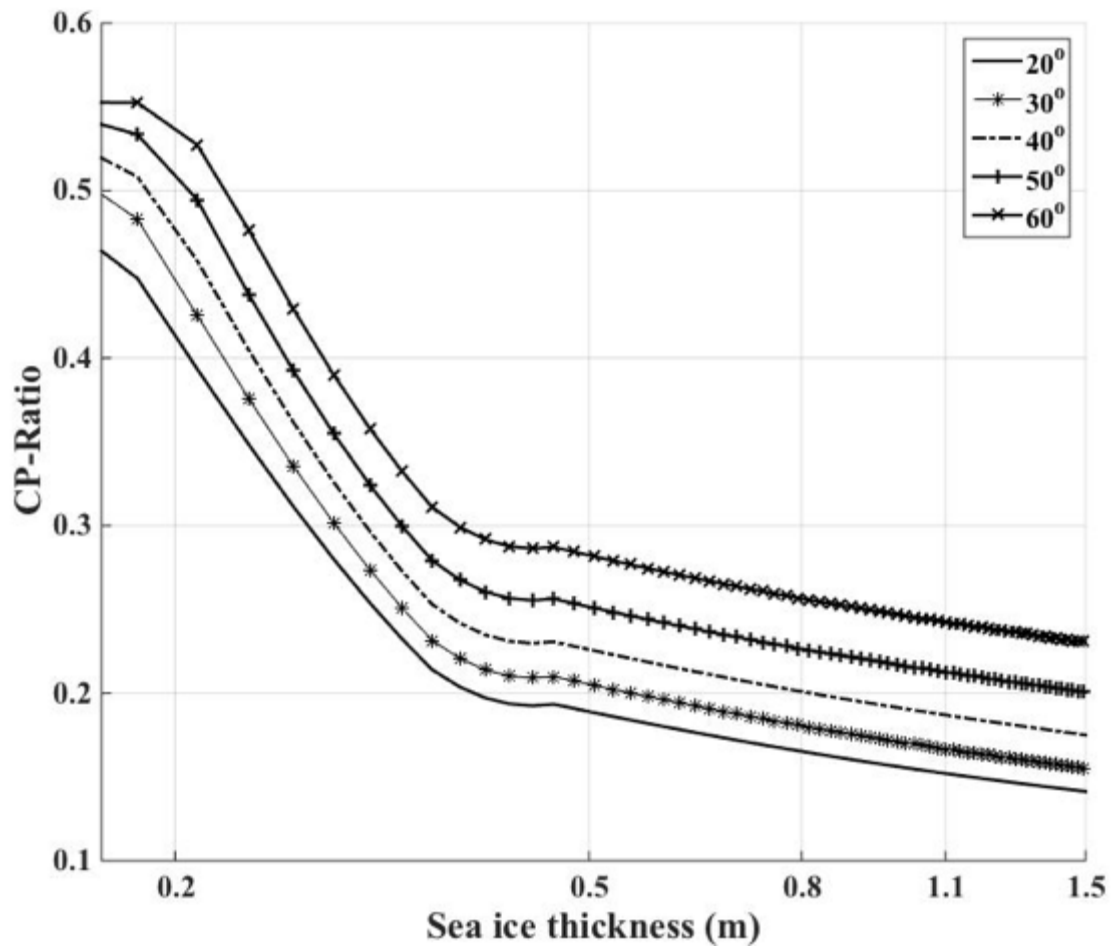
1  
 2 Figure 2. *CP-Ratio* as a function of dielectric constants for different  $\sigma$  and incidence  
 3 angle= $30^\circ$ . The results for other incidence angles follow the similar trends.  
 4



5  
 6 Figure 3. Structure and geometric model of the configuration of sea ice.  
 7



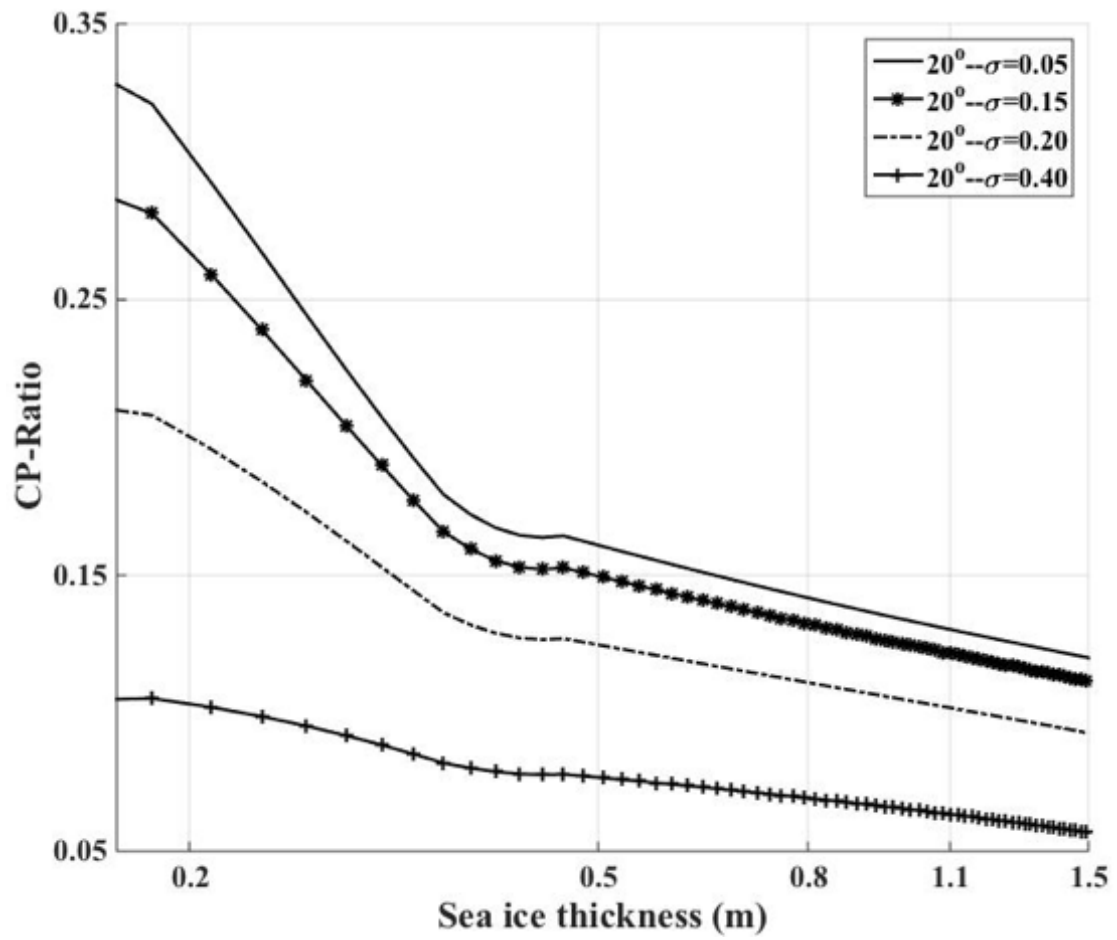
1  
 2 Figure 4. The simulated sea ice growth process. Blue: sea ice thickness; red: sea ice  
 3 surface temperature; green: the volume fraction of brine inclusions.  
 4

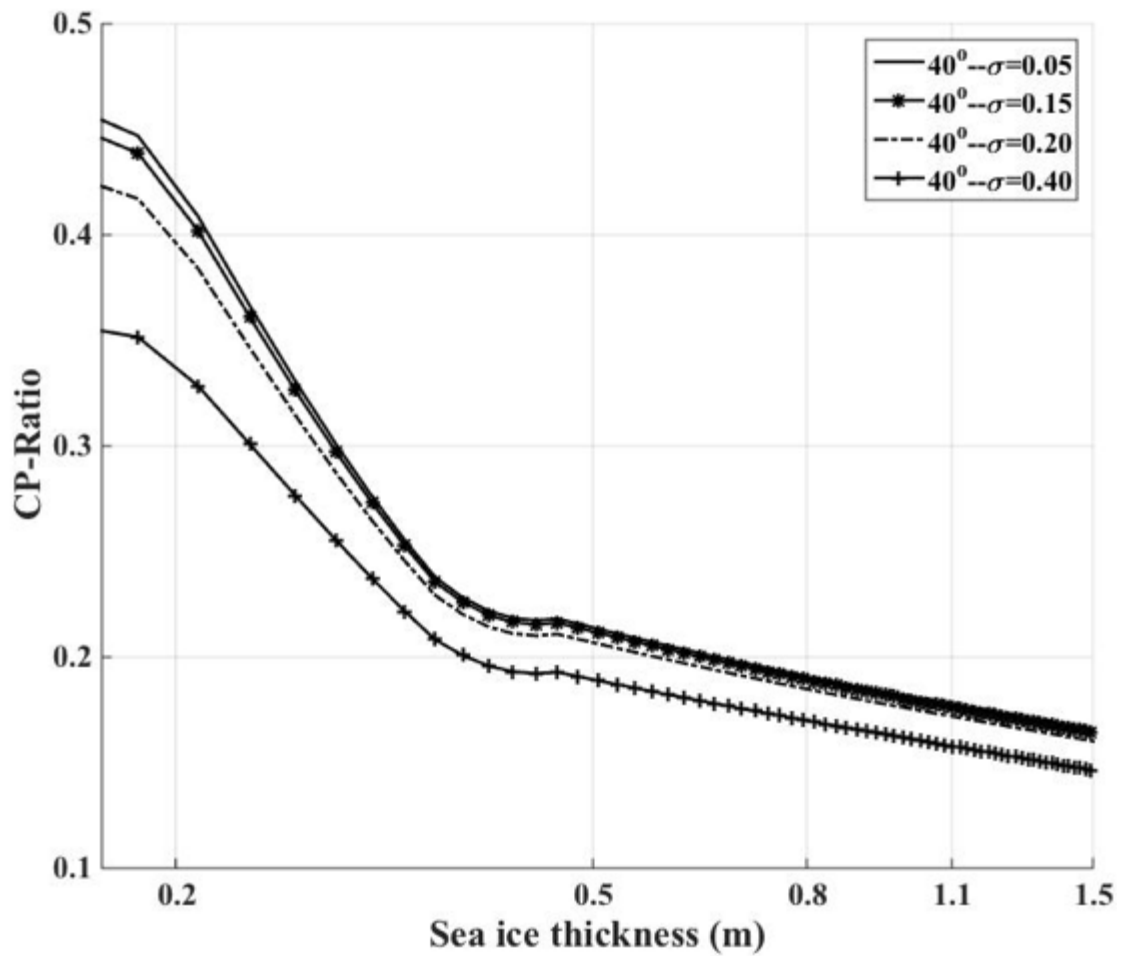


1  
2  
3  
4  
5  
6

Figure 5. The relationship between *CP-Ratio* and ice thickness at different incidence angles for C-band radar (*x*-axis in log scale). The incidence angle varies from 20° to 60°. The small-scale roughness parameters are set to  $s=0.11$  cm and  $l=0.54$  cm (case 3), the standard deviation of the surface slope  $\sigma=0.1$ .

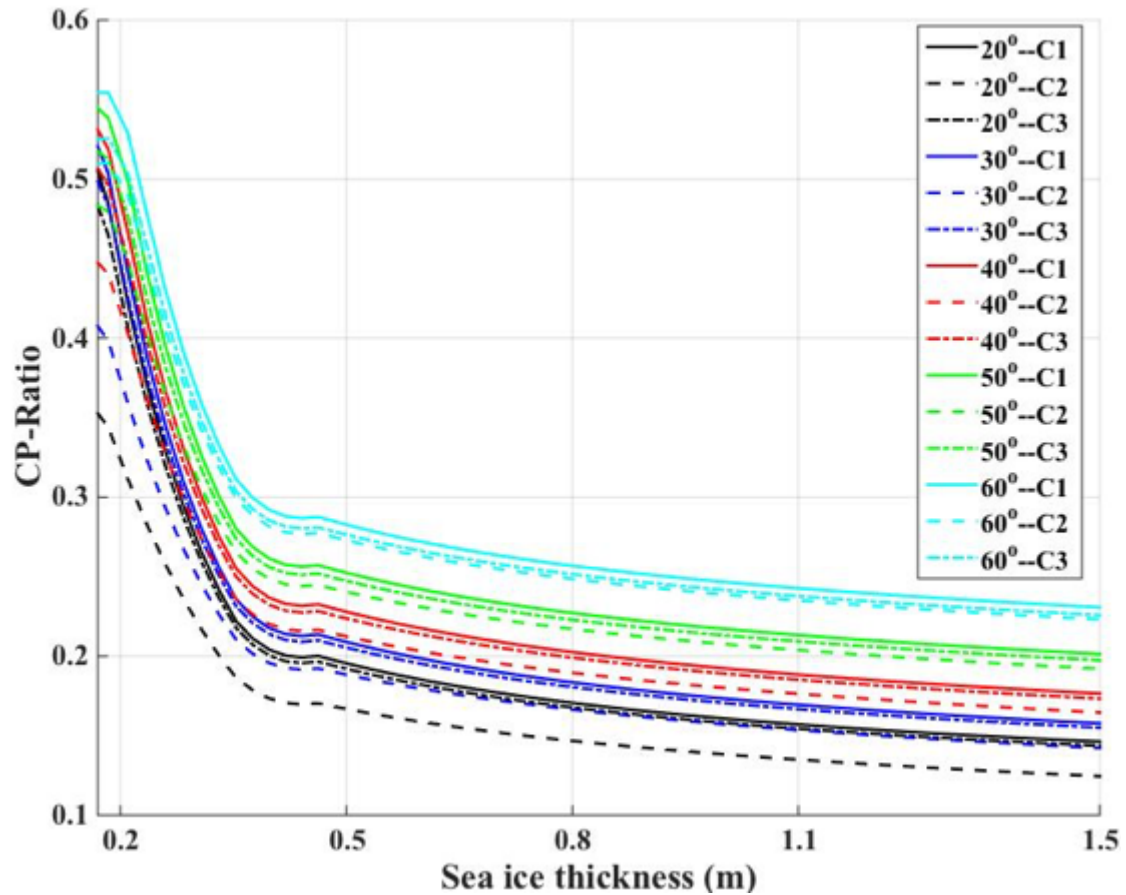






1  
2  
3  
4  
5  
6

Figure 6. Sensitivity of *CP-Ratio* to the standard deviation of the surface slope  $\sigma$  (x-axis in log scale). The standard deviation of the surface slope  $\sigma$  varies from 0.05 to 0.4, while the small-scale roughness is fixed at  $s=0.12$  cm and  $l=1.45$  cm (case 2). Top figure is for  $20^\circ$  incidence angle and bottom is for  $40^\circ$  incidence angle.



1

2 Figure 7. Sensitivity of *CP-Ratio* to the small-scale roughness (x-axis in log scale).

3 The standard deviation of the surface slope  $\sigma$  is fixed at 0.1. Black, blue, red, green

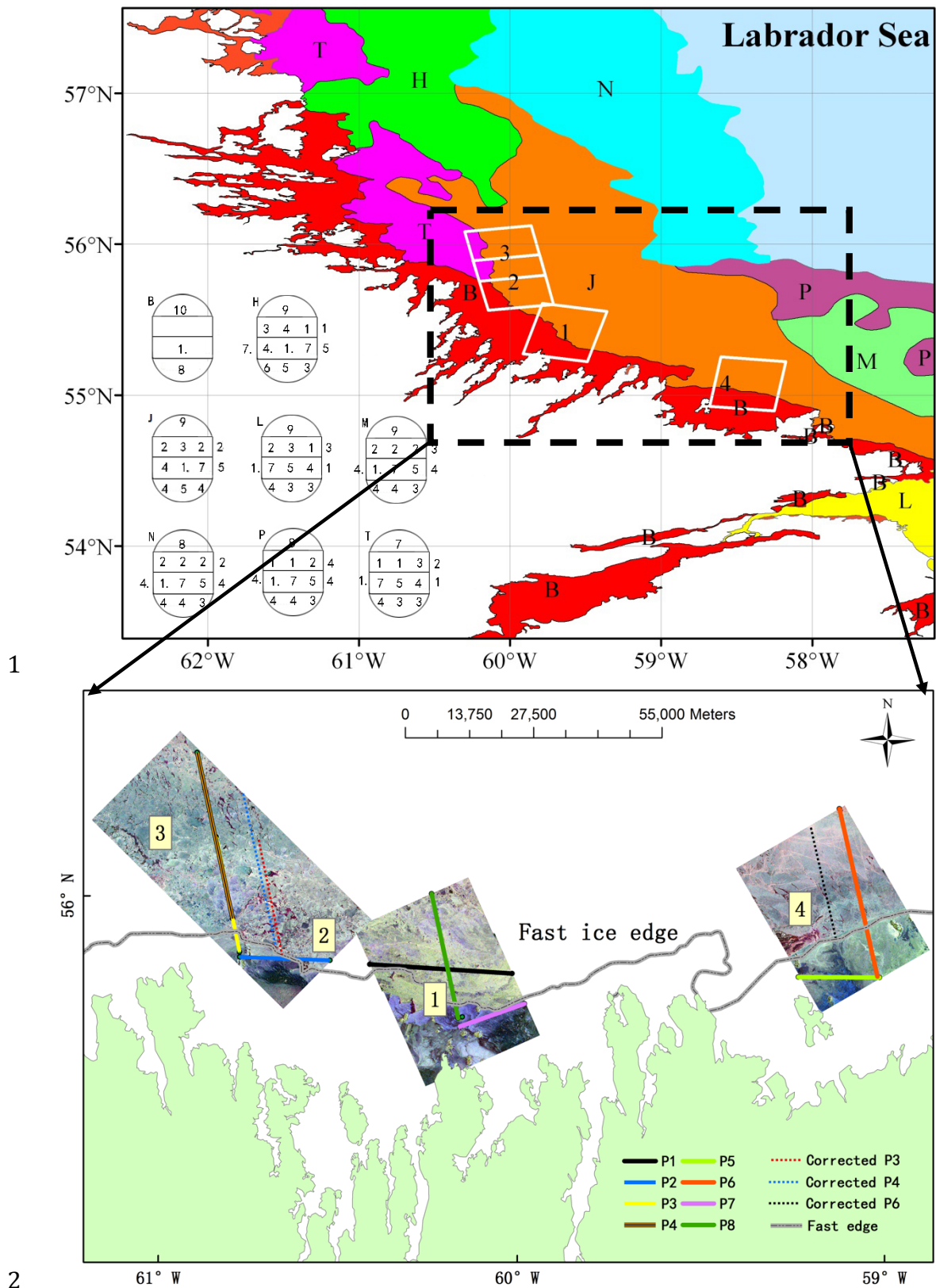
4 and cyan color are for 20°, 30°, 40°, 50°, and 60° incidence angles, respectively. In

5 the legend, C1, C2 and C3 denote the three cases of small-scale surface roughness

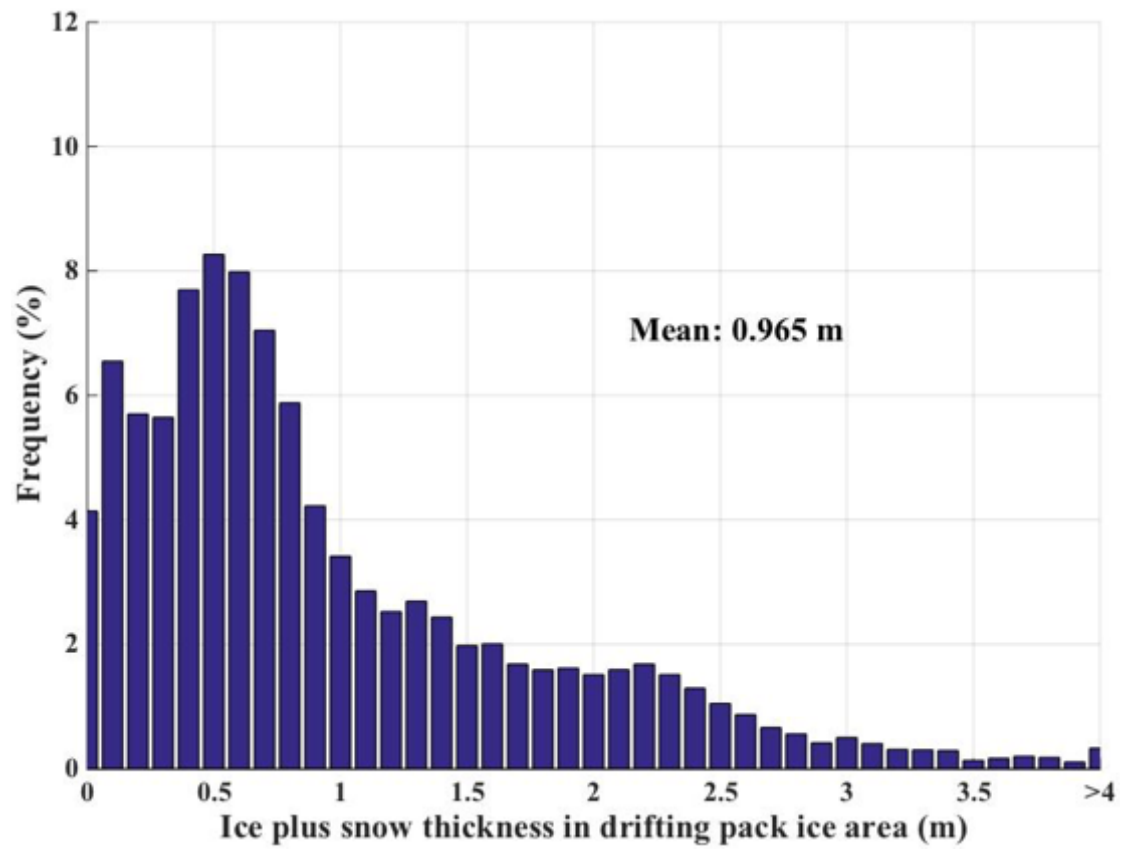
6 respectively (C1:  $s=0.031$  cm,  $l=1.26$  cm; C2:  $s=0.12$  cm,  $l=1.45$  cm; C3:  $s=0.11$  cm

7  $l=0.54$  cm)

8

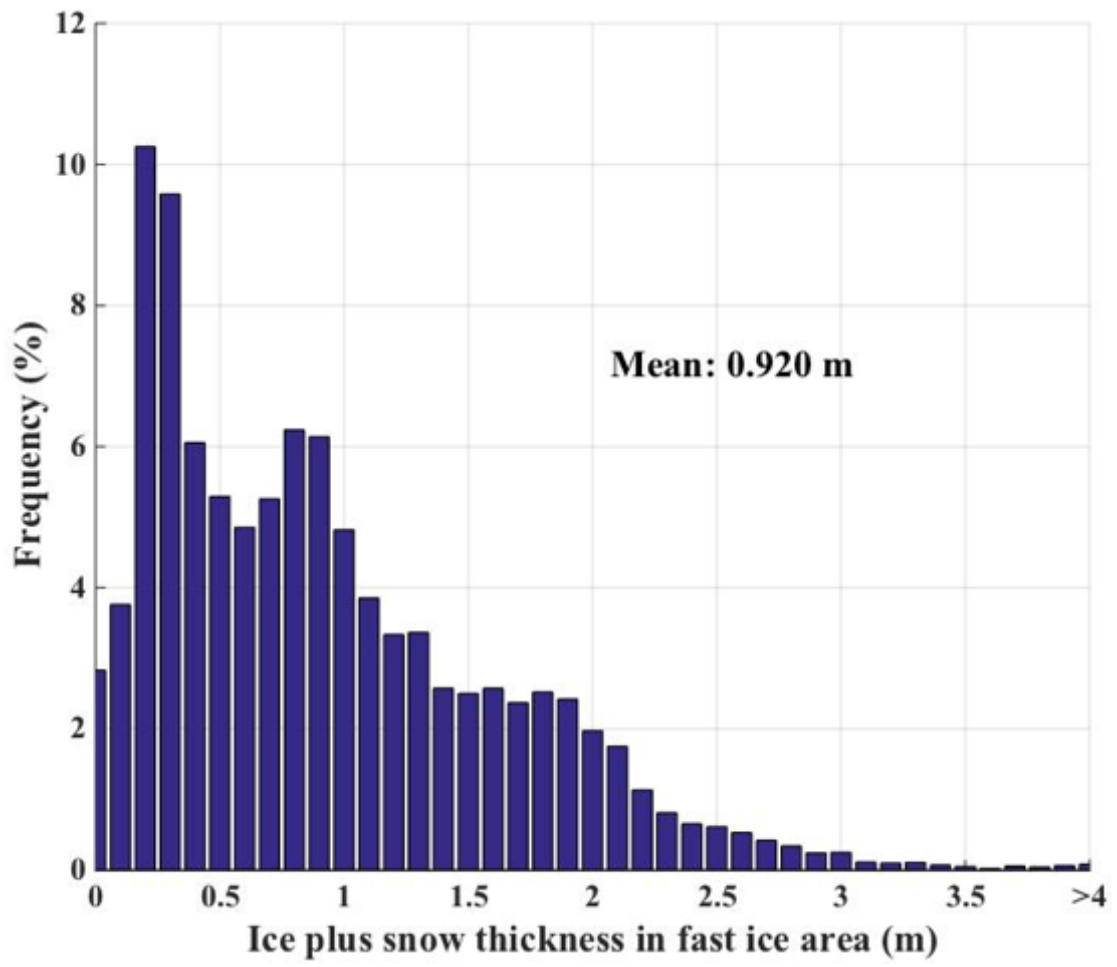


1  
2  
3 Figure 8. Location of the study site in the Labrador Sea, with Pauli RGB (HH+VV for  
4 blue, HH-VV for red, and HV for green) decompositions of the RADARSAT-2  
5 images © MDA. The specifications of the used SAR data are given in Table 3.



1  
2

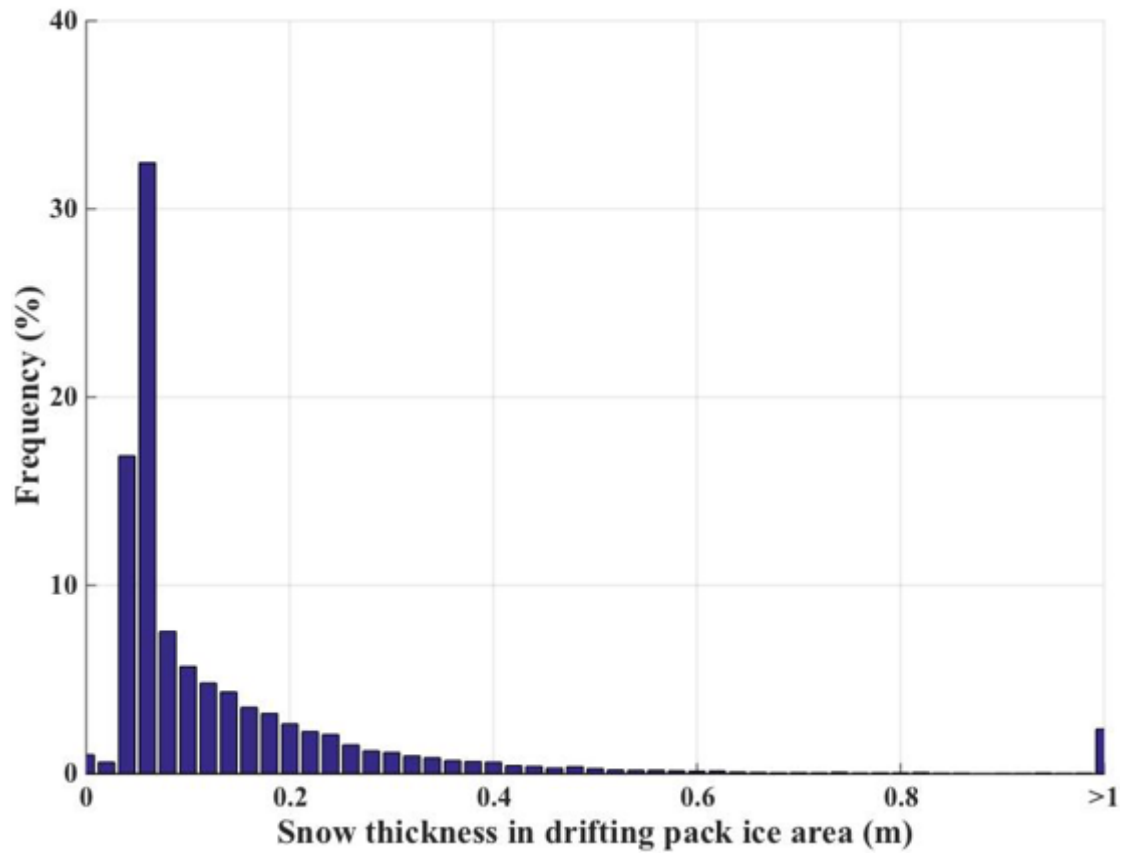
(a)



1

2

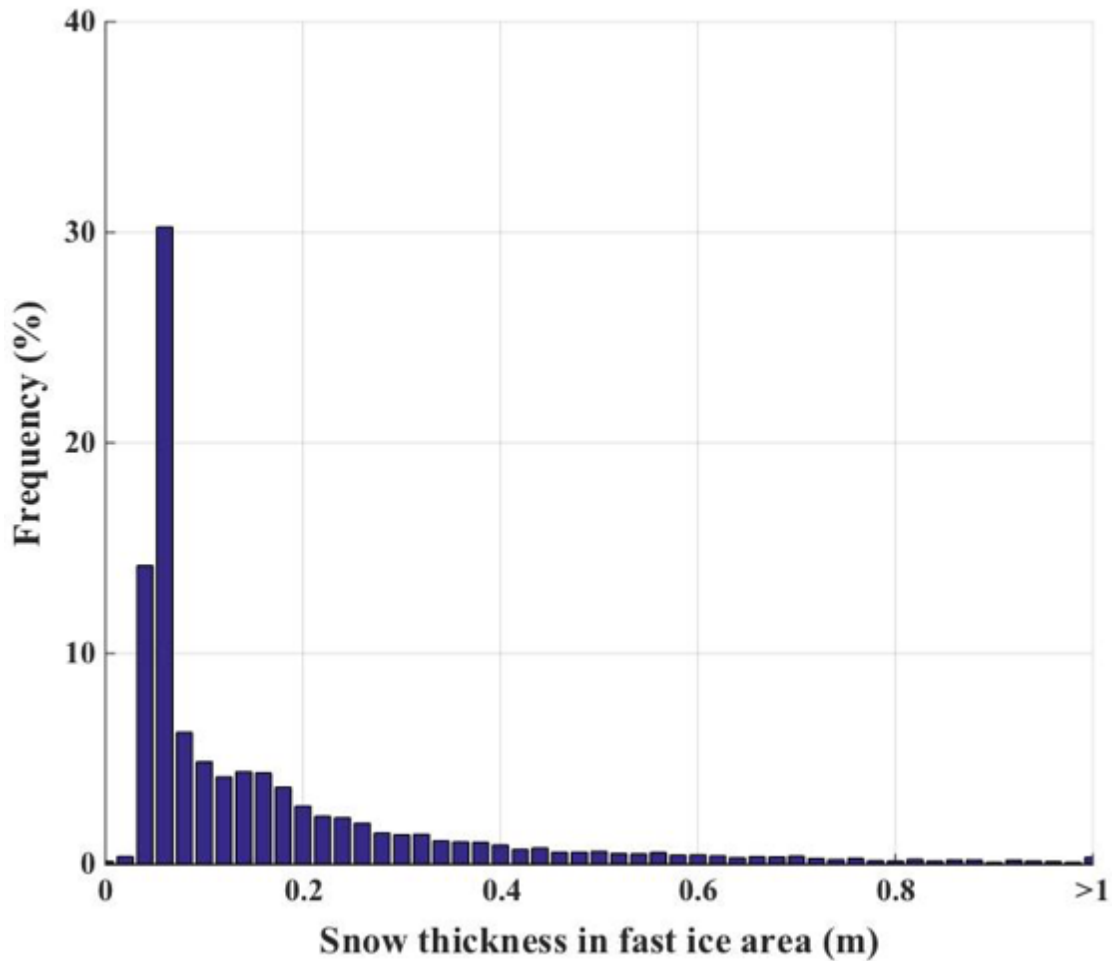
(b)



1

2

(c)

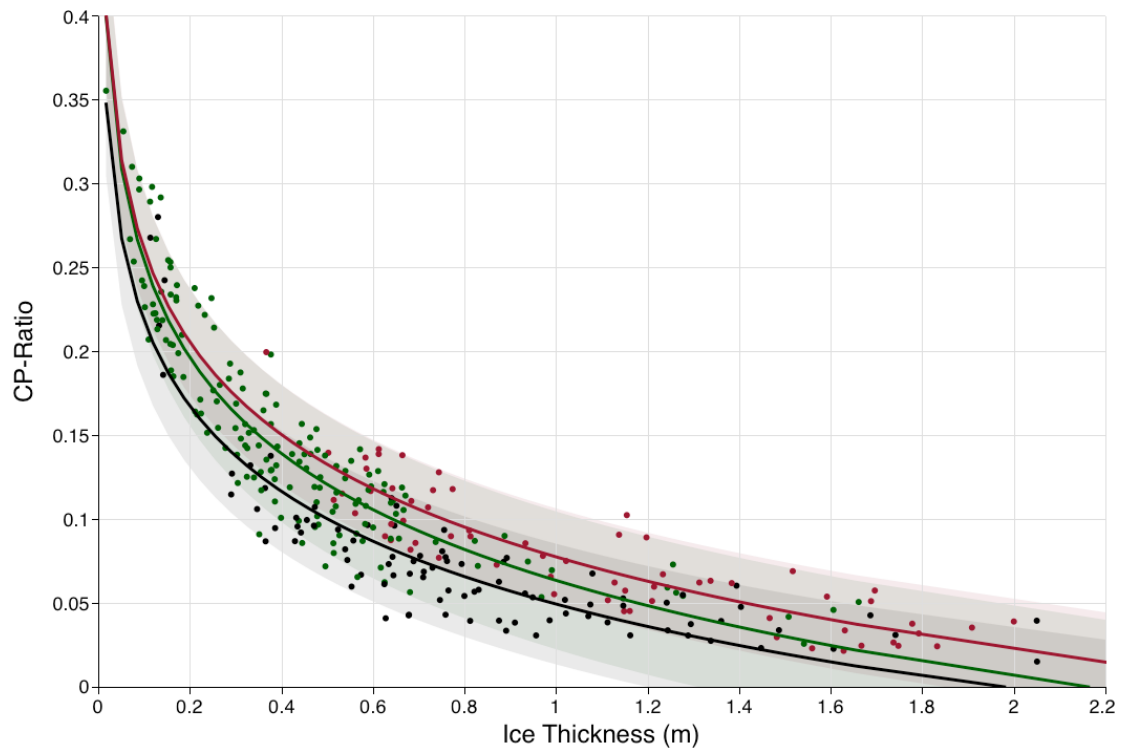


1  
2  
3  
4  
5  
6  
7  
8  
9  
10  
11

(d)

Figure 9. Histogram of ice and snow thickness in the Labrador Sea. (a) and (b): Ice plus snow thickness collected with EMS in the pack ice (a) and in the fast ice area (b). (c) and (d): Snow thickness collected with GPR in the pack ice (c) and in the fast ice area (d). The bin widths of ice and snow thickness and snow thickness are 0.1 m and 0.02 m respectively. The histograms of the fast ice area are generated from flight tracks of P1, P2, P5, and P7. The histograms of the pack ice area are generated from flight tracks of P3, P4, P6, and P8. These histograms include both level and deformed ice.



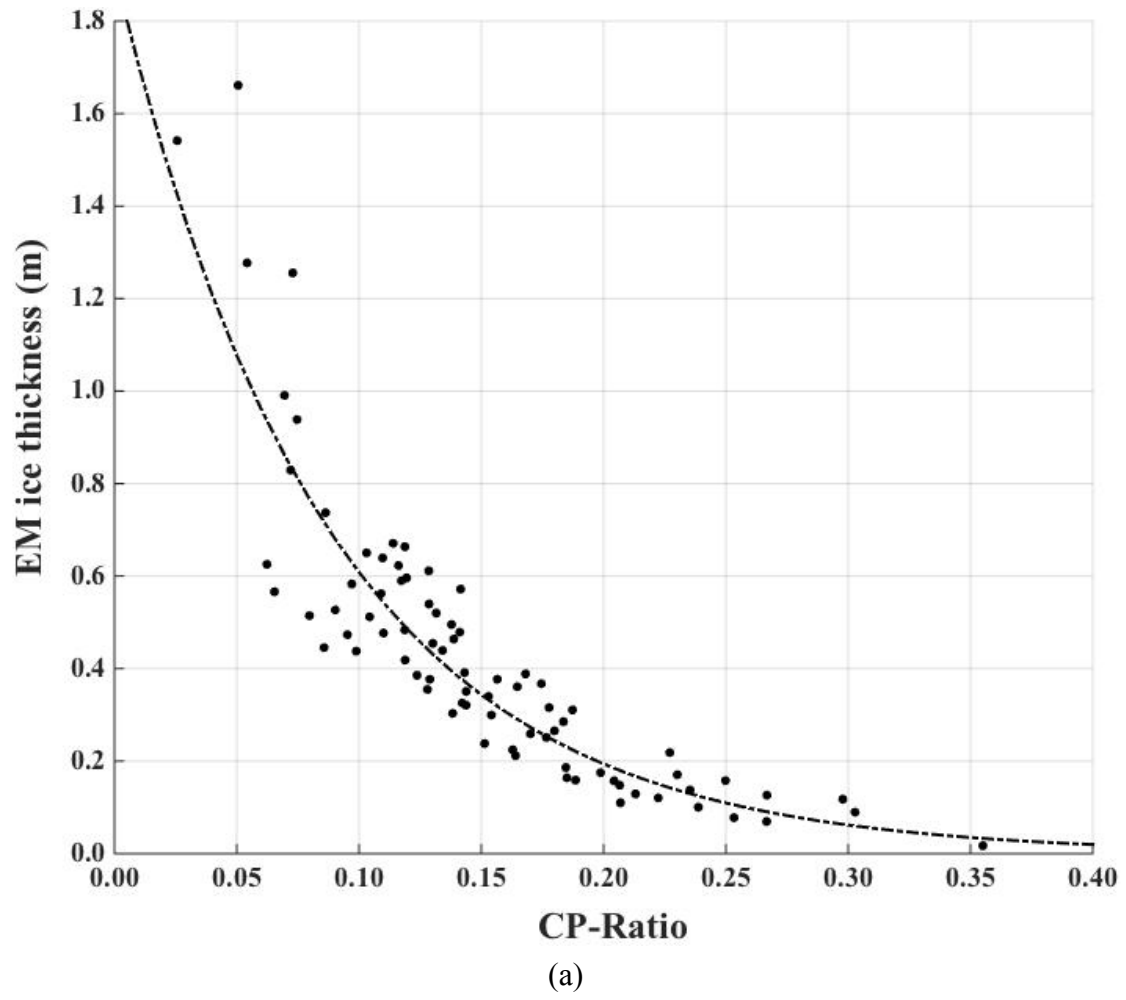


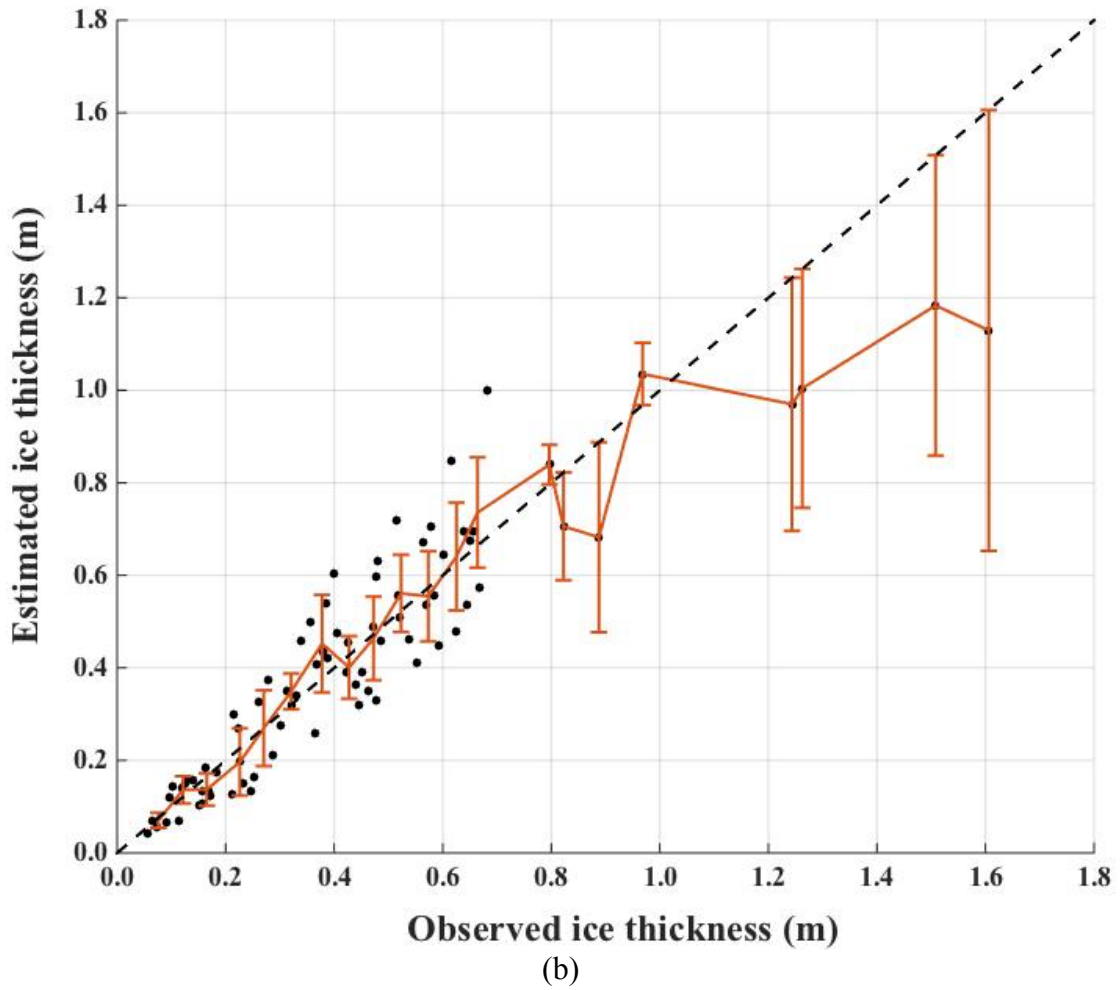
1

2 Figure 10. Regressions relating ice thickness to *CP-Ratio* at different incidence angles.

3 The solid lines represent the fits, dashed lines the 90% confidence intervals. The black,  
4 green and red colors are used for the incidence angles of  $29^\circ$ ,  $42^\circ$  and  $49^\circ$ ,  
5 respectively.

6





1  
2  
3  
4  
5  
6  
7  
8

Figure 11. (a) Relationship between the *CP-Ratio* and the observed EM sea thickness.  
 (b) Comparison between the observed and estimated ice thicknesses, and the errorbars show the standard deviation with respect to the observation data for every 0.05 m segment of ice thickness.